Perigenual and Subgenual Anterior Cingulate Afferents Converge on Common Pyramidal Cells in Amygdala Subregions of the Macaque

Abbreviated title: pgACC-sgACC Afferent Interactions

Kelly, EA [1], Thomas, VK [2], Indraghanty, A [1], and Fudge, JL [1, 3]

Affiliations:
1 Department of Neuroscience, University of Rochester, Rochester NY 14642
2 Department of Pharmacology and Physiology, University of Rochester, Rochester NY 14642
3 Department of Psychiatry, University of Rochester, Rochester NY 14642

Corresponding Author:
Del Monte Institute of Neuroscience
University of Rochester Medical Center
601 Elmwood Avenue
Rochester, NY 14642
julie_fudge@urmc.rochester.edu
585 275 4535

Number of Pages: 30
Number of Figures: 8
Number of Tables: 1
Number of Words in Abstract: 250
Number of Words in Introduction: 627
Number of Words in Discussion: 1302

Conflict of Interest

The authors declare no competing financial interests.

Acknowledgments

This work was funded through the support of the National Institute of Mental Health R01MH63291 (J.L.F.). We thank Nanette Alcock for assistance with histology and immunohistochemistry.

Abstract

The subgenual (sgACC) and pregenual (pgACC) anterior cingulate are important afferents of the amygdala, with different cytoarchitecture, connectivity, and function. The sgACC is associated with arousal mechanisms linked to salient cues, while the pgACC is engaged in conflict decision-making, including in social contexts. After placing same-size, small volume tracer injections into sgACC and pgACC of the same hemisphere in male Macaques, we examined anterogradely labeled fiber distribution to understand how these different functional systems communicate in the main amygdala nuclei at both mesocopic and cellular levels. The sgACC has broad-based termination patterns. In contrast, the pgACC has a more restricted pattern which was always nested in sgACC terminals. Terminal overlap occurred in subregions of the accessory basal and basal nuclei, which we termed 'hotspots'. In triple-labeling confocal studies, the majority of randomly selected CAMKIIα (+) cells (putative amygdala glutamatergic neurons) in 'hotspots' received dual contacts from the sgACC and pgACC. The ratio of dual contacts occurred over a surprisingly narrow range, suggesting a consistent, tight balance of afferent contacts on postsynaptic neurons. Large boutons, which are associated with greater synaptic strength, were approximately 3 times more frequent on sgACC versus pgACC axon terminals in 'hotspots', consistent with a fast ‘driver’ function. Together, the results reveal a nested interaction in which pgACC ('conflict/social monitoring’) terminals converge with the broader sgACC ('salience') terminals at both the mesoscopic and cellular level. The pre-synaptic organization in 'hotspots' suggest that shifts in arousal states can rapidly, and flexibly influence decision-making functions in the amygdala.

Significance statement

The subgenual (sgACC) and perigenual cingulate (pgACC) have distinct structural and functional characteristics and are important afferent modulators of the amygdala. The sgACC is critical for arousal, while the pgACC mediates conflict-monitoring, including in social contexts. Using dual tracer injections in the same monkey, we found that sgACC inputs broadly project in the main amygdala nuclei, whereas pgACC inputs were more restricted and nested in zones containing sgACC terminals (‘hotspots’). The majority of CAMKIIα + (excitatory) amygdala neurons in 'hotspots' received converging contacts, which were tightly balanced. pgACC and sgACC afferent streams are therefore highly interdependent in these specific amygdala subregions, permitting 'internal arousal' states to rapidly shape responses of amygdala neurons involved in conflict and social monitoring networks.

Introduction

Emotional processing involves coding sensory data as biologically relevant, or ‘salient’, for the organism to survive. The amygdala codes the emotional relevance of complex sensory inputs through an intricate network of intrinsic and extrinsic connections. In humans and monkeys, the amygdala is especially sensitive to salient stimuli of a ‘social’ nature (i.e. facial expression, vocal expressions; Gothard et al., 2007; Rutishauser et al., 2011; Mosher et al., 2014; Wang et al., 2014; Rutishauser et al., 2015; Wang et al., 2017), which supports survival in highly interdependent social groups. The same neural ensembles in monkey amygdala can code reward associated with both nonsocial and social stimuli (Munuera et al., 2018), indicating a common or overlapping circuitry available for coding ‘salience’ and ‘social’ cue evaluation.

In both human and nonhuman primates, the amygdala is a heterogenous structure with evolutionary expansion of 'cortical-like' nuclei that communicate directly with the cortex (in contrast to the ‘extended amygdala’ structures, which mainly regulate hypothalamus and brainstem; Stephan et al., 1987). The basal and accessory basal nuclei of the amygdala are the key sites of higher processing through strong, reciprocal connections with the prefrontal cortex (PFC), in particular the anterior cingulate (ACC) (Carmichael and Price, 1995; Ghashghaei et al., 2007; Cho et al., 2013; Sharma et al., 2020). These ‘cortical-like’ nuclei contain pyramidal projection neurons and interneuron populations similar to the cortex.

In the human and monkey, amygdala-ACC networks are implicated in flexibly and appropriately modulating reward learning (Zhang et al., 2013), threat and extinction learning (Klavir et al., 2013; Reddan et al., 2018) and learning from social cues (Allsop et al., 2018; Munuera et al., 2018; Dal Monte et al., 2020). The ACC-amygdala connection develops gradually over childhood and adolescence (Gabard-Durnam et al., 2014; Gee et al., 2018), is influenced by early life experience, and is vulnerable to dysregulation in a host of human psychiatric illnesses (Johansen-Berg et al., 2008; Kim et al., 2011; Burghy et al., 2012).

The primate ACC, including that in human, has multiple subdivisions based on cytoarchitectural, connectional, and functional features (Vogt et al., 2005). The ‘subgenual’ ACC (sgACC), and ‘pregenual’ ACC (pgACC) are most connected with the amygdala (Cho et al., 2013; Sharma et al., 2020). The sgACC (areas 25/14c) is involved in monitoring emotional arousal and autonomic states (Vogt et al., 2005; Rudebeck et al., 2014). In contrast, the pregenual ACC (areas 24/32) is involved in ‘conflict’ decision-making, particularly in social contexts (Modirrousta and Fellows, 2008; Amemori and Graybiel, 2012; Livneh et al., 2012; Apps et al., 2016; Lockwood and Wittmann, 2018; Palomero-Gallagher and Zilles, 2018).

98 In a previous broad-based study that evaluated 'top-down' projections from the PFC to
99 amygdala using retrograde tracer injections, we found that cortical inputs to the amygdala co-
100 project with one another in a hierarchical manner, dictated by the relative granularity of the
101 cortical region of origin (Cho et al., 2013). The least differentiated cortices (including the sgACC)
102 form a 'foundational circuit' throughout the basal and accessory basal nuclei, upon which
103 increasingly complex information from more differentiated cortical regions (e.g. pgACC) is
104 'layered' in more restricted amygdala subregions.
105 In the present study, we took an anterograde tracing approach to examine the idea that
106 'social and conflict monitoring' nodes of the ACC (i.e. the pgACC) that project to the amygdala
107 would always occur in the context of more foundational 'salience' inputs (sgACC) in the
108 amygdala. We placed injections into area 25/14c (sgACC 'salience/arousal') and area 24 and
109 32 (pgACC, 'social and conflict monitoring') nodes of the ACC in the same animal and examined
110 their patterns of segregation and overlap in specific amygdala nuclei. Then, in regions where
111 sgACC and pgACC terminals overlapped, we further investigated the patterns of convergence
112 or segregation onto pyramidal cell populations using high resolution confocal techniques.
113 Finally, we characterized terminal bouton size from each afferent source.

114 Materials and Methods

115 Experimental Design

116 A total of 7 injections sites in 5 animals were analyzed for this study: 2 single injections
117 into the sgACC, 1 single injection into the pgACC, and 2 pairs of combined injections in the
118 sgACC/pgACC (Table 1). Using the criteria of Carmichael and Price (Carmichael and Price,
119 1994), we designated injections that involved areas 25/14c as subgenual anterior cingulate
120 (sgACC) and injections into area 32 and/or 24b as perigenual anterior cingulate (pgACC),
121 respectively. A small injection of a different tracer was placed into the sgACC and pgACC of the
122 same hemisphere in the macaque in two animals. After sectioning and processing of the brains
123 for tracers using immunocytochemistry, we mapped the distribution of anterogradely labeled
124 afferent fibers within amygdala subregions and used these macroscopic maps to identify
125 regions of terminal segregation and overlap in the amygdala. We then conducted triple
126 immunofluorescent analyses aimed at examining the relationship of axon contacts onto
127 presumptive glutamatergic neurons in regions of terminal overlap. The relative size of synaptic
128 boutons associated with the sgACC and pgACC in regions of overlap were conducted in single-
129 labeled, adjacent sections using stereologic methods.

130 Animals and surgery

131 Injections were stereotaxically placed in 5 male *Macaque fascicularis* (Worldwide
132 Primates, Tallahassee, FL USA) weighing between 4.3kg and 5.5 kg (Table 1). Prior to surgery
133 and tracer injection, a T2 anatomical MRI scan using a custom head coil (0.5 x 0.5 x 0.88
134 millimeter resolution) was acquired on each subject. Thus, each subject had unique
135 coordinates based on individual anatomy. Seven days prior to surgery, animals began a daily
136 course of perioperative gabapentin (25 mg/kg) for preventative pain management. On the day of
137 surgery, the monkey was sedated with intramuscular ketamine (10mg/kg) and then intubated,
138 maintained on 1.5% isoflurane, and stabilized in a surgical stereotaxic apparatus. A craniotomy
139 was performed under sterile conditions. In four animals, small injections (40 nl) of bidirectional
140 tracers tetramethylrhodamine (fluoruby, FR) and fluorescein (FS) were pressure injected over a
141 ten-minute period into the sgACC and/or pgACC of the same hemisphere, using coordinates
142 calculated from the T2 MRI atlas created for that animal. Because of the relatively small terminal
143 field resulting from 40 nl injections in the pgACC (see Results), a single injection of 150 nl was
144 pressure injected into pgACC of a fifth animal for comparison (case MF54FS). For all injections,
145 the syringe was left in place for 20 minutes after each injection to prevent tracking of the tracer
146 up the injection track. Only one tracer injection of each type was made per animal. Following
147 placement of planned injections, the bone flap was replaced, and the surgical site was closed.
148 Post-operative daily monitoring of animals for signs of discomfort was conducted and
149 gabapentin tapered accordingly.

150 Tissue preparation

151 Twelve to fourteen days post-surgery, the animals were placed into a deep coma with
152 pentobarbital (initial dose 20 mg/kg via intravenous line). They were sacrificed by intra-cardiac
153 perfusion using 0.9% saline containing 0.5 milliliters of heparin sulfate (200ml/min for 15-20
154 minutes), followed by cold 4% paraformaldehyde in 0.1M phosphate buffer, pH 7.2 (PB)
155 (200ml/min for 15-20 minutes). Following brain extraction, brains were postfixed overnight in 4%
156 paraformaldehyde solution, then submerged sequentially in 10%, 20%, and 30% sucrose
157 solutions until they sank in each. Brains were sectioned on a freezing, sliding microtome into
158 40um sections. Each section was placed sequentially in 24-compartment slide boxes containing
159 cold cryoprotectant solution (30% sucrose and 30% ethylene glycol in 0.1 M PBS) and stored at
160 -20°C.

161 Single label immunocytochemistry (ICC)

162 To assess the location of anterogradely labeled fibers in amygdala subregions, we first
163 stained 1:8 sections through the amygdala for each tracer. We selected adjacent sections to
164 stain with cresyl violet or immunostain for NeuN in order to localize injection sites in the frontal
165 cortex. In the amygdala, adjacent sections were stained for acetylcholinesterase (AChE)
166 activity. AChE histochemistry shows clear demarcations of nuclear boundaries in the non-
167 human primate amygdala (Amaral and Bassett, 1989) (Fig. 1) For cases with dual injections,
168 three 1:24 adjacent compartments of tissue through the amygdala were selected: one for the
169 sgACC tracer, one for the pgACC tracer, and one intervening compartment for AChE staining.
170 Sections selected for ICC were rinsed in 0.1MPB, pH 7.2, with 0.3% Triton-X (PB-TX) overnight.
171 The following day, tissue was treated with endogenous peroxidase inhibitor for five minutes and
172 then thoroughly rinsed with PB-TX, and placed in a blocking solution of 10% normal goat serum
173 in PB-TX (NGS-PB-TX) for 30 minutes. Following rinses in PB-TX, tissue was incubated in
174 primary antisera to FR (1:1000, Invitrogen, rabbit) or FS (1:2000, Invitrogen, rabbit) for ~96
175 hours at 4°C. Tissues were then rinsed with PB-TX, blocked with 10% NGS-PB-TX, incubated in
176 biotinylated secondary anti-rabbit antibody, and then incubated with avidin-biotin complex
177 (Vectastain ABC kit, Vector Laboratories, Burlington, ON Canada). After rinsing, the tracer was
178 visualized with 2,2'-diaminobenzidine (DAB, 0.05mg/ml in 0.1M Tris-buffer). Sections were
179 mounted out of mounting solution (0.5% gelatin in 20% ETOH in double distilled water) onto
180 subbed slides, dried for 3 days, and coverslipped with DPX mounting media (Electron
181 Microscope Sciences, Hatfield, PA). Additional sections were also selected, immunostained and
182 then counterstained with Nissl to confirm fiber localization in specific nuclei, including the
183 intercalated cell islands. Immunostaining with NeuN was conducted similar to the procedure
184 described above, using anti NeuN (1:5000, EMD Millipore, mouse) and the avidin biotin
185 reaction.

186 Triple immuno-fluorescent labeling for tracers and CAMK-IIα

187 To determine the relationship of anterogradely labeled fibers from the peri- and
188 subgenual ACC into the amygdala, and their relationship with glutamatergic amygdala neurons,
189 we performed triple immunofluorescent staining for each tracer and calmodulin-dependent
190 protein kinase II (CAMK-IIα)(McDonald et al., 2002) on an additional series through the
191 amygdala in animals with paired injections. Optimization and specificity of fluorescent staining
192 for all antigens was first conducted in single labeling experiments, with reference to the

193 permanently labeled compartments for tracer (above) and CAMKIIα. Sections were rinsed in
194 0.1M PB, pH 7.2, with 0.3% Triton-X (PB-TX) overnight. The following day, tissue was treated
195 with endogenous peroxidase inhibitor for 30 minutes and then thoroughly rinsed with PB-TX and
196 placed in a blocking solution of 10% normal donkey serum in PB-TX (NDS-PB-TX) for 1 hour.
197 Following rinses in PB-TX, tissue was incubated in 3% NDS-PB-TX primary antisera to FR
198 (1:1000, Invitrogen #A6397, *made in rabbit*), FS (1:500, Invitrogen, #A11095, *made in goat*) and
199 CAMK-IIα (1:1,000, Millipore #05-532, *made in mouse*) for ~96 hours at 4°C. Tissues were then
200 rinsed with PB-TX, blocked with 3% NDS-PB-TX and first incubated in biotinylated secondary
201 anti-mouse antibody (1:200, Vector Labs, CAMK-IIα amplification) overnight at 4°C. Tissues
202 were visualized following pooled incubation with donkey anti- rabbit Alexa Fluor 568 (1:200, FR
203 visualization), donkey anti-goat Alexa Fluor 488 (1:100, FS visualization) and Streptavidin 647
204 (1:200, CAMK-IIα visualization). Tissue was mounted out of 0.1M PB, pH 7.2 and cover-slipped
205 with Prolong Gold anti-fade mounting media (Invitrogen).

206 Analysis

207 *Charting of anterograde fiber labeling in specific amygdala subregions.*

208 For all cases, charting of the distribution of anterogradely labeled fibers throughout the
209 entire amygdala was first done on single-labeled, permanently stained tissue. Anterogradely
210 labeled fibers for each case were visualized using an Olympus BX51 microscope equipped with
211 a darkfield light source. Fibers were manually traced using an attached camera lucida drawing
212 tube using a 4X and 10x objectives. Putative terminal fibers were characterized as thin
213 processes with boutons. Thick labeled fibers without beaded processes were classified as fibers
214 of passage and were not traced. Paper traces were scanned on a flat-bed scanner at high-
215 resolution. Images were imported, stitched together and digitized using Adobe Photoshop CC.
216 AChE-stained adjacent sections were projected onto anterograde traces using a JENA projector
217 and nuclei borders were manually traced with the aid of landmarks within the tissue (i.e. blood
218 vessels) and transferred onto digital files using a drawing tablet interfaced with the Adobe
219 Illustrator CC. Tracer labeled sections and adjacent AChE labeled sections were placed into
220 separate layers of in each file and aligned. Final image digitation and post-processing was
221 performed using Adobe Illustrator CC. For paired injections in the same animal, the relationship
222 of the anterogradely labeled fibers resulting from each injection site, and their localization in
223 specific amygdala subregions, was done by turning off and on the visibility of layers. Regions of

224 the main cortical-like nuclei that contained either segregation (‘non-overlap’) or overlap
225 (‘hotspots’) of pgACC and sgACC labeled terminals were identified.
226 To quantify the density of anterograde fiber distribution in regions of overlap, we
227 combined dark field microscopy with ImageJ (FIJI) analysis (Schneider et al., 2012). From
228 cases with paired injections, low power images (4x objective) of ‘hotspots’ were first collected
229 using dark field microscopy, and then re-captured at higher magnification (20X objective), using
230 blood vessels and other landmarks to align ROIs across sections. Using Image J, the mean
231 background density was determined from three unlabeled areas of each image. Images were
232 manually thresholded to isolated fiber labeling (0-255 density scale; 0=black, 255=white), then
233 converted to a binary scale (divided by 255; labeled regions=1, unlabeled regions=0). Original
234 images were than multiplied by the binary masked image to obtain a density value for the
235 image. The final density measurement was obtained after mean background subtraction.

236 *Confocal capture and analysis of interactions between tracer-labeled fibers and CAMK-IIα*
237 *positive cells*

238 Cases with paired injections in the sgACC and pgACC and their regions of labeled fiber
239 overlap in the amygdala (subregions that contained glutamatergic neurons) (‘hotspots’) were
240 further assessed using high power (confocal) microscopy. We used a semi-automated algorithm
241 to detect and quantify relative numbers of tracer labeled boutons on amygdala CAMK-IIα
242 positive cells. While synaptic contacts can only be confirmed at the electron microscope level,
243 we devised a method to examine the relationship of putative 'contacts' and their relationship to
244 one another using confocal methods. Triple-immunofluorescent images were collected on a
245 Nikon A1R HD Laser Scanning Confocal with NIS-Elements (Center for Advanced Light
246 Microscopy and Nanoscopy) software using tissue landmarks on adjacent AChE-stained
247 sections such as blood vessels for alignment, focusing on regions of interest (ROIs) where
248 tracer labeled fibers overlapped at the light microscopic level. The following excitation lasers
249 (ex) and emission filters (em) were used for confocal imaging: Alexa Fluor 488; ex 488, em
250 525/50, Alexa Fluor 568; ex 561, em 595/50, Streptavidin 647; ex 640, em 650 LP. Overview
251 images were collected using a 20x/0.75 NA Nikon Plan Apochromat VC objective to locate ROIs
252 in regions of tracer labeled fiber overlap, and z-series stacks were selected and collected using
253 a 60x/ 1.49 NA Nikon Apochromat TIRF objective (xy pixel size of 0.17 micron; z-step size of
254 0.3 micron). 2-3 ROIs per ‘hotspot’ were collected per slide in each nucleus (n=2-3 slides;
255 rostral to caudal extent of the amygdala) for each experimental case.

256 Projection images were analyzed with Imaris 9.6 software (Bitplane). Within each
257 collected image stack (approximately 6-9 stacks per ROI per animal), ten CAMK-IIα positive
258 cells were randomly selected for analysis. XYZ coordinate locations for each analyzed cell were
259 carefully logged. In the 3D module, CAMK-IIα labeling was visualized using the "*surface*
260 *rendering*" option (grain size=0.345 um diameter). The "smoothing" tool was disabled, as this
261 introduces an artificial uniformity to the cell surface. Next, using the interactive software
262 histogram of Cy5 voxels (volumetric pixels), a threshold was selected to include as much of the
263 neuronal soma and proximal dendrites as possible while excluding any background. A second
264 threshold (interactive size threshold) was next applied to exclude any further extraneous
265 background labeling while still retaining the true volume of the labeled cell. Final renderings
266 were then analyzed in 3D and looked at from all angles. In instances where the labeling was
267 disjointed but clearly part of the actual cell, segments were linked, resulting in an n=10 cells per
268 image.
269 Fibers were analyzed using the "*spot rendering*" option. In the "slice view", fiber
270 thickness was checked (a line measurement across the entire thickness of the fiber), resulting in
271 a final size diameter of 2 um for all cases. The sensitivity for selected spots was adjusted using
272 the automatically generated interactive histogram based on voxel size. We selected an area on
273 the histogram to accurately detect as many boutons as possible without creating artifacts.
274 Identical coordinates used during the "*surface rendering*" step were then applied to the "*spot*
275 *rendering*" steps to ensure a 1:1 registration between the analyzed locations (CAMK-IIα
276 containing cells) for detection and analysis of tracer labeled boutons. This step was conducted
277 for each tracer labeled bouton, and individually overlaid on the CAMKIIα-positive surface
278 rendering.
279 Once the combined CAMK-IIα 'surface' rendering and 'spot' renderings for tracer labeled
280 boutons were constructed, we sought to determine the proportion of putative glutamatergic
281 neurons contacted by tracer-labeled spots, including the proportion of CAMK-IIα containing
282 neurons receiving dual-contacts. To do this, we used the "shortest distance" module to filter out
283 all spots that were more than 0.5um from the cell surface. In the Imaris software, spot/surface
284 contacts are based on a measurement from the center of the spot (radius) to the edge of the
285 rendered surface object. As 'spots' were calculated as 2um, a radius of 1um would determine all
286 spots "touching" a surface. Fiber boutons located close to CAMK-IIα cells but not in actual
287 contact, may have an apparent voxel overlap due to the inherent resolution limits of light
288 microscopy (a blurring of fluorescent edge resolution that extends beyond the actual true
289 surface boundary). False-positive contacts can be controlled for by requiring a minimum number

290 of overlapping voxels for an object to be classified as a true contact (Wouterlood et al., 2007).
291 Our analysis was restricted to a maximum object to surface distance of 0.5um (at least a 50/50
292 overlap of spot and surface objects; Fig. 2) to create a relatively stringent inclusion criteria for
293 assessing 'synaptic contact'. Each CAMK-IIα (+) cell was analyzed in 3D and manual counts
294 were performed in each fluorescent channel. We sought to determine a range of cell-contact
295 types; including (i) no contacts, (ii) individual tracer contacts, and (iii) cells that contained dual
296 contacts (single tracer contacts on the same cell). We present our results as (i) the proportion
297 of pgACC/sgACC contacts on all CAMK-IIα cells and (ii) the percentage of contact type (see
298 description above) onto CAMK-IIα (+) cells across amygdalar nuclei. For CAMK-IIα positive
299 neurons receiving dual contact, we also analyzed the ratio of pgACC to sgACC contacts on
300 each individual cell, presented as the percentage of neurons with different ratios of
301 pgACC:sgACC contacts per 'hotspot' as well as the frequency of those contacts.

302 *Analysis of bouton size from pgACC and sgACC.*

303 To examine the relative size of axonal boutons from the pgACC and sgACC, we used
304 unbiased stereologic methods to survey the basal and accessory basal nucleus 'hotspots' where
305 overlapping terminals were found in each case. For comparison with 'hotspots', regions with
306 non-overlapping sgACC (sgACC non-OL) terminals were also assessed (Fig. 5, dark blue).
307 Using adjacent sections immunostained for the relevant tracer placed either in the sgACC or
308 pgACC, the general terminal distribution in each 'hotspot' was drawn using a 2x (Plan, NA 0.05
309 ∞/-) objective. To sample under 100x (UPlanFl, NA 1.3) oil immersion objective, sampling
310 parameters were: grid size 300 x 300, dissector height of 2um and a z-height of 5 um, resulting
311 in sufficient sampling to yield a coefficient of error < 0.10. Axonal varicosities and terminal-like
312 structures are considered synapses, as previous confirmed by electron microscopic methods
313 (Ashaber et al., 2020). Both were counted using systematic, random sampling strategies in
314 single-labeled adjacent slides for each tracer. The nucleator method (isotropic), which assumes
315 sphericity of the structure, was applied to measure each putative synaptic structure along the Z
316 axis, in the sampling frame (StereoInvestigator, Microbrightfield Bioscience, Williston, VT).
317 Results were expressed in um^3. Frequency histograms were created for each tracer in each
318 area, and assessed for shape, spread, and percent of synaptic terminals > 0.52 μm^3 (equivalent
319 to 1 um diameter).

320 Statistics

321 Statistical analyses were performed using Graphpad Prism software (V9.0.2 for
322 Windows, LaJolla, California). A two-way ANOVA was used to compare tracer-labeled density
323 measurement in regions of fiber overlap ('hotspots"). A two-tailed unpaired student t-test was
324 used to compare the total number of contacts in each injection group across amygdalar region.
325 Similarly, a two-tailed unpaired student t-test was used to compare pgACC/sgACC ratio means
326 across amygdalar nuclei. A 2x3 two-way ANOVA investigated the relationship of contact type on
327 injection site (pgACC vs sgACC) and ROI (ABmc vs Bi). A two-way ANOVA was used to
328 compare pgACC/sgACC ratio bin means across amygdala nuclei and injection sites. A one-way
329 ANOVA was used to compare rostral/caudal differences in dual contacts. All statistical tests
330 were corrected for multiple comparisons using Tukey's multiple comparison test (Tukey's HSD)
331 where appropriate. $P<0.5$ was deemed statistically significant. Error bars are presented as
332 standard error of the mean.

333 **Results**

334 Primate amygdala

335

336 The nonhuman primate amygdala spans 5-6 mm. in the rostrocaudal plane, and its
337 nuclei shift in shape and cellular characteristics within this space (Fig. 1. A-D).
338 Acetylcholinesterase (AChE) is used to follow cytoarchitectural boundaries between and within
339 nuclei (Amaral and Bassett, 1989). The 'deep' nuclear group of the amygdala includes the
340 lateral, basal, and accessory basal nuclei, and also referred to as 'cortical-like' nuclei due to
341 specific cellular and connectional characteristics (Carlsen and Heimer, 1988). These large
342 nuclei contain pyramidal neurons and interneurons, and are intimately connected with broad
343 regions of the prefrontal cortex (Ghashghaei et al., 2007; Cho et al., 2013). They are relatively
344 expanded in primate species compared to the rodent, and with this expansion comes increased
345 subnuclear organization which is only partially described here. The lateral nucleus is divided
346 into dorsal, ventral intermediate, and ventral subdivisions with differing cellular features and
347 AChE staining. The accessory basal nucleus consists of the magnocellular (ABmc) and
348 parvicellular (ABpc) subdivisions, which have high and low levels of AChE, respectively. There
349 is also a 'sulcal' subdivision of the accessory basal nucleus (ABs) that is medial and posterior
350 relative to the other subdivisions. The basal nucleus is subdivided into magnocellular (Bmc),
351 intermediate (Bi) and parvicellular subdivisions (Bpc), which have a decreasing gradient of cell

352 size and AChE staining. The basal nucleus is surrounded by the paralaminar nucleus (PL),
353 which is most prominent at its ventral boundary, but has almost absent AChE staining and not
354 seen in these preparations. The intercalated cell islands are inhibitory neurons, that are lodged
355 in the major fiber tracts that surround the 'cortical-like' nuclei. These small clusters of
356 GABAergic neurons (Pitkanen and Amaral, 1993) also cannot be appreciated with AChE
357 staining but are easily seen in cresyl violet preparations (Fig 1 E-F).
358 The anterior and posterior cortical nuclei (CoA and CoP, respectively), the medial
359 nucleus, and the periamygdaloid cortex form the 'superficial' amygdala region. The
360 amygdalohippocampal (AHA) region is an AChE-rich nucleus that forms a broad transitional
361 region with the hippocampus, and is also composed of glutamatergic neurons and interneurons.
362 In the dorsal amygdala, the central nucleus is situated caudally, and in is divided into medial
363 and lateral central core subdivisions. It is separated from the striatum by a relatively broad,
364 heterogeneous amygdalostriatal area (Fudge and Tucker, 2009). The medial and central
365 amygdaloid nuclei are considered part of the 'extended amygdala' macrostructure, and are
366 largely GABAergic.
367
368 Injection site placement
369
370 The sgACC comprises areas 25c and 14c of the ACC; the pgACC comprises areas 32
371 and 24 (Fig. 3A and B, Table 1). The sgACC is agranular cortex that is defined by a lack of
372 granular layer IV. sgACC injections were mainly in area 25, with slight involvement of 14c only
373 in case 53FR. Case 37FR was located most rostrally, with Cases 50FR, 46FS, and 53FR at
374 progressively caudal levels (Table 1). Injections into the pgACC, which is slightly more
375 differentiated (Fig. 3A), were in either area 24b (Case 46FR) or area 32r/32c (Case 53FS) or
376 encompassed both area 24b and the entire rostrocaudal extent of 32 in one case with a large
377 single injection (Case 54FS). Figure 3C shows examples a single sgACC injection (case 37FR)
378 and Figures 3-D1 shows dual pgACC injection (case 53FS) and sgACC injection (case 53FR),
379 each with adjacent sections stained to localize placement with respect to cytoarchitectural
380 profiles.
381

382 General topography of sgACC and pgACC inputs to the amygdala

383 All injections into the sgACC resulted in broad distribution of anterogradely labeled
384 fibers, specifically in the medial nucleus (M), the lateral nucleus (L), the magnocellular

385 subdivision of the accessory basal nucleus (ABmc), the magnocellular and intermediate
386 subdivisions of the basal nucleus (Bmc, Bi), the medial subdivision of the central nucleus (CeM)
387 and the amygdalostriatal areas (Fig. 4A-C, blue). Scattered labeled fibers existed in the
388 parvicellular subdivision of the basal nucleus (Bpc) and accessory basal nucleus (ABpc),
389 amygdalohippocampal area (AHA), and in the intercalated islands (Fig. 1E-F) that surrounded
390 the basal nucleus, consistent with previous studies (Freedman et al., 2000). There were no
391 apparent rostrocaudal differences in labeled fiber distribution, despite slight rostrocaudal
392 differences in sgACC injection placement. Moreover, inclusion of the area 14c (in case 53FR)
393 did not alter the distribution of labeled fibers in the amygdala.
394 In general, tracer injections into the pgACC resulted in fewer labeled terminals than
395 sgACC injections, and the distribution was more restricted (Fig. 4D-F, red). Because pgACC
396 injections resulted in a more restricted pattern of anterogradely labeled terminals, compared
397 with sgACC injections, we placed a single large injection encompassing area 32/24b (case
398 54FS) using three times the normal injection volume (150 nl) as a comparison. For this
399 relatively large injection, labeled terminal fibers were still qualitatively less dense, and more
400 confined, than sgACC injections using 40 nl (not shown). Labeled fibers were found in the
401 accessory basal nucleus, magnocellular subdivision (ABmc) and the basal nucleus,
402 intermediate and magnocellular subdivisions (Bi, Bmc) and in the medial and lateral
403 subdivisions of the central nucleus (CeM, CeLcn,respectively), and amygdalostriatal area, with
404 few to no labeled fibers found in other regions including the intercalated islands.

405 <u>pgACC and sgACC labeled fibers overlap in amygdala 'hotspots'</u>

406 Paired injections, matched for tracer volumes, were first mapped throughout the entire
407 amygdala using adjacent sections containing labeled fibers from each ACC node (Cases 46 and
408 Case 53, Fig. 5-1). The paired injection cases each had an injection into sgACC; case 46 had a
409 companion injection in pgACC (area 24b), and case 53 had a companion injection in pgACC
410 area 32. Tracers injected into the pgACC and sgACC had been 'reversed' in case 46 and 53 to
411 control for possible effects of tracer transport (fluorescein injection into sgACC /fluororuby
412 injections into pgACC for case 46; the reverse was done for case 53). Resulting maps were
413 consistent with the patterns of labeled fibers seen in single-injection cases (Fig. 5-1), but
414 permitted examination of patterns of segregation and convergence of labeled terminals from
415 each site in the same animal.
416 Our analysis focused on all amygdala nuclei containing glutamatergic projection
417 neurons (i.e. excluded the medial and central nucleus) (Fig. 5 A-F). As in single injection cases,

418 sgACC labeled terminals targeted more nuclei (the accessory basal nucleus, basal nucleus,
419 lateral nucleus, and AHA) compared to the pgACC (Fig. 5, A-C and D-F, blue). Labeled
420 terminals from the pgACC injections targeted mainly the accessory basal nucleus and the basal
421 nucleus, with no labeled fibers in the lateral nucleus or AHA (Fig. 5, A-C and D-F, red). Within
422 the basal nucleus, the sgACC labeled fibers were found in all subdivisions, while pgACC
423 labeled terminals were largely confined to the Bi (and to a lesser extent, the Bmc). In the
424 accessory basal nucleus, sgACC labeled terminals extended into both the magnocellular and
425 parvicellular subdivisions, whereas pgACC labeled fibers were confined to the magnocellular
426 accessory basal nucleus. These results were consistent with previous retrograde data (Cho et
427 al., 2013).
428 Overlap of pgACC and sgACC terminals occurred in areas where the pgACC had
429 terminals: the intermediate subdivision of the basal nucleus and accessory basal nucleus
430 (magnocellular subdivision) (Fig. 5A-C, and D-F, green outlines). That is, pgACC terminals
431 were nested in the overall sgACC terminal distribution. We designated these regions of overlap
432 'hotspots'. Regions where sgACC terminals did not overlap with pgACC labeled fibers were
433 designated as segregated, or 'non-overlapping' regions, and also demarcated (dark blue
434 outlines).
435 In 'hotspots', the relative density of labeled terminals following sgACC injections was
436 generally higher than for pgACC injections, regardless of tracer used (Fig 5G-I). Some sgACC
437 labeled beaded fibers were thicker, there were many thin, varicose labeled fibers (Fig. 5G).
438 pgACC labeled fibers appeared thin and more diffuse (Fig. 5H). Quantification of fiber density
439 confirmed significantly denser distributions of fibers originating from sgACC in both ABmc and
440 Bi ('hotspots') compared to those originating from pgACC (Fig. 5I; sgACC:ABmc vs
441 pgACC:ABmc= p=0.0003; sgACC:Bi vs pgACC:Bi= p=0.0018; Two-way ANOVA with Tukey's
442 multiple comparisons test). Further, sgACC-originating fiber density was significantly higher
443 regardless of 'hotspot' region (sgACC:ABmc vs pgACC:Bi= p=0.0054; sgACC:Bi vs
444 pgACC:ABmc=p=0.0001).

445 <u>Most CAMKIIα (+) cells in 'hotspots' receive dual contacts</u>

446 For cases with paired injections (cases 46 and 53), we then conducted triple-labeling for
447 each tracer and CAMKIIα (a marker of pyramidal neurons in the amygdala (McDonald et al.,
448 2002)). We used confocal methods to determine the degree of fiber 'contact' onto putative
449 excitatory neurons in both ABmc and Bi 'hotspots' where labeled terminals from both the sgACC

450 and pgACC converged (Fig. 6A-B; see Methods). Thresholding of randomly selected
451 CAMKIIα(+) cells and tracer labeled fibers was completed in separate channels, and overlaid.
452 Randomly selected CAMK-IIα(+) cells in each 'hotspot' in each case were examined for
453 contacts with either sgACC or pgACC tracer (+) boutons (Fig. 6C-D). Given some variability in
454 labeled fiber distribution across the rostrocaudal extent of the ABmc and Bi for all
455 tracers/injections at the macroscopic level, we first examined whether there were differences in
456 numbers of pgACC and sgACC contacts across the entire rostrocaudal expanse in each animal.
457 No rostrocaudal differences were found (see Fig. 6-1 for rostral-caudal raw data; Two-way
458 ANOVA with Tukey Multiple Comparisons test, $F(5,16)= 0.2176$, $p=0.9495$), and results of all
459 sections were grouped for each animal (Fig. 6-2, pooled raw data). For all CAMK-IIα(+) cells
460 examined (n=300), there were no significant differences in the number of pgACC and sgACC
461 contacts (sgACC: 247 contacts in ABmc, 244 contacts in Bi; pgACC: 346 contacts in ABmc, 271
462 contacts in Bi; ANOVA with Tukey's Multiple Comparisons test; $F(3,4)=0.9985$, $p=0.4795$; n.s.).
463 The ratio of pgACC to sgACC labeled contacts was approximately equal in both the ABmc and
464 Bi 'hotspots (Fig.6E, n= 150 total cells ABmc, n=150 total cells Bi, two-tailed students t-test;
465 $p=0.2525$; n.s.).
466 We then explored the extent to which pgACC and sgACC contacts converged on the
467 same CAMK-IIα(+) cells in each area. The majority of randomly selected CAMK-IIα(+) neurons
468 had contacts from both the sgACC and pgACC, in both ABmc and Bi regions (Fig. 6F, Two-way
469 ANOVA with Tukey multiple comparisons test; $F(7,24)= 9.634$; DUAL vs all other contact
470 profiles= ***= $p<0.0001$). Relatively lower proportions of CAMK-IIα(+) neurons had no contacts
471 from either projection or had contacts from a single projection. There were no significant
472 differences in the distribution of dual-contact CAMK-IIα(+) neurons in the rostrocaudal plane
473 (One-Way ANOVA with Tukey multiple comparisons tests, Case 46:ABmc= $F(2,4)=11.85$,
474 $p=0.0609$; Case 46:Bi= $F(2,3)=6.231$, $p=0.0855$; Case 53:ABmc= $F(2,5)=5.136$, $p=0.0613$,
475 $p=0.0613$; Case 53:Bi= $F(2,6)=0.5588$, $p=0.5990$).

476 <u>The proportion of pgACC to sgACC dual contacts are tightly balanced</u>

477 Since the majority of CAMK-IIα(+) neurons in 'hotspots' had dual contacts, we calculated
478 the relative weighting of sgACC and pgACC contacts on individual dually contacted cells, and
479 the distribution of the ratios of pgACC-to-sgACC contacts throughout the ABmc and Bi
480 populations (Fig. 7 A-B, Fig. 7-1). Ratios of contacts from each area onto individual CAMK-
481 IIα(+) neurons ranged from 0 to 3.5. The majority of dual pgACC: sgACC contact ratios for both

482 the ABmc and Bi were in a narrow 1.0-1.5 range, suggesting a relatively tight balance of inputs
483 onto individual pyramidal neurons in most cases. Given this narrow range, we pooled our data
484 and performed quantification based on ratio bin counts (Fig. 7C). Quantitative comparisons of
485 ratio bin counts display significantly higher counts in the range of 1-1.5 when compared to every
486 other bin (*=p<0.05, ****= p<0.001, one-way ANOVA with Tukey multiple comparisons post hoc
487 test).

488 sgACC and pgACC synaptic bouton volumes

489 We next examined bouton volumes from the sgACC and pgACC in each 'hotspot' as an
490 approximation of synaptic 'strength' (Petrof and Sherman, 2013). sgACC non-overlapping (non-
491 OL) terminals in the lateral nucleus and AHA were examined for comparison. Data were
492 collected on terminal boutons and bouton*s 'en passant'* using stereologic methods in adjacent,
493 single labeled sections. In all areas assessed, the majority of boutons were significantly less
494 than 0.52 um^3 volume (equivalent 1um diameter) for sgACC and pgACC afferents (Fig. 8 A-E;
495 multiple comparison tests were performed to compare small vs. large bouton across region and
496 case. In all situations, there were significantly more small boutons compared to large boutons
497 (p=0.008 [J46], p=0.015 [J53], p=0.005 [pooled])). However, in 'hotspots' in the ABmc and Bi,
498 there was a higher frequency of relatively large terminals for the sgACC (Fig. 8-1 and 8-2).
499 Using >0.52 um^3 (> 1 um diameter) as a cut-off for 'large' boutons, we found that the sgACC
500 terminals that overlapped pgACC-containing sites had significantly more large boutons (27-
501 31%) compared to the pgACC (9-10%) (Fig. 8F; *sgACC*: J46 (total large boutons/total) =
502 194/617; M53 (total large boutons/total) = 142/509; *pgACC*: J46 (total large boutons/total) =
503 29/307; M53 (total large boutons/total) = 61/595; p=0.003; One-Way ANOVA with Tukey's
504 multiple comparison test, F(2,3)=96.18= p=0.0019; sgACC vs pgACC= p=0.0003). 'Large'
505 bouton comparisons from the same afferent source did not differ significantly across the ABmc,
506 Bi (p=0.0.3739, Two-way ANOVA, F(2,2)=1.674), suggesting a common feature of sgACC
507 inputs in 'hotspots'. In contrast, sgACC non-OL areas had significantly fewer large boutons,
508 suggesting a specific feature in 'hotspots' (Fig 8F, Tukey Multiple Comparisons test following
509 one-way ANOVA; sgACC vs non-OL= p=0.0023).

510 **Discussion**

511 In broad-based studies, we previously showed that prefrontal-amygdala paths are
512 organized in hierarchical arrays, dictated by the degree of laminar differentiation of the cortex

513 (Cho et al., 2013). To examine this relationship in a more focused way and at the cellular level,
514 we placed anterograde tracer injections into two different nodes of the ACC that have
515 progressive laminar features (pgACC>sgACC), and distinct connections and functions
516 (Carmichael and Price, 1995 ; Rushworth et al., 2013; Neubert et al., 2015; Palomero-Gallagher
517 et al., 2015). In this study, we found that at the 'meso-scale' that pgACC afferent terminals are
518 always 'nested' in broader sgACC terminals in the basal and accessory basal nuclei, confirming
519 previous retrograde results, and elucidating connectional principles of the two ACC-amygdala
520 microcircuits.
521 At the cellular level, we found that the majority of CAMIIα (+) amygdala neurons
522 (putative projection neurons) in 'hotspots' of convergence were co-contacted by terminals from
523 the sgACC and pgACC. This was true regardless of whether the 'hotspot' was in the ABmc or
524 Bi. Despite the size of the 'hotspots' in the large primate samples, there were no rostrocaudal
525 differences for these findings. Another key finding is that the ratio of pgACC-to-sgACC contacts
526 was highly consistent within and across 'hotspots' and fell mainly in the range of 1.0-1.5. This
527 suggests a general consistency in the relationship in pgACC:sgACC afferent balance onto
528 common post-synaptic cells in regions of convergence, at least in young Macaques. Finally,
529 sgACC terminals in 'hotspots' were more likely to have large boutons, compared to pgACC
530 terminals, in the zones of convergence, suggesting possible differences in transmission speed
531 and efficiency.
532
533 Layering of amygdala subcircuits
534
535 The agranular sgACC is strongly interconnected with the midline thalamus,
536 hypothalamus and periacqueductal gray, all of which mediate arousing and autonomic
537 components of emotional responses (Van Hoesen et al., 1993; Vogt, 2005; Rudebeck et al.,
538 2014). The sgACC has therefore been considered a core node in the ‘somatic’ marker
539 hypothesis, which states that covert signals from the body (such as autononomic features and
540 visceral sensations) are important in shaping emotions and, eventually, action (Damasio, 1996;
541 Chudasama et al., 2013). In contrast, the pgACC (Area 24/32) sits directly and dorsally
542 adjacent to the sgACC and is more organized in its laminar construction. However, the pgACC
543 does not have direct connections to the internal milieu via midline connections like the sgACC,
544 although it shares many of the same ‘limbic’ connections and receives input from the sgACC
545 (Barbas et al., 1999; Joyce and Barbas, 2018; Sharma et al., 2020). The pgACC plays a
546 prominent role in rapid assessment of competing choices (including 'conflictual’ choices) and

547 decision-making, based on studies in monkeys (Rudebeck et al., 2006; Amemori and Graybiel,
548 2012; Pryluk et al., 2020) and in the human (Etkin et al., 2006; Modirrousta and Fellows, 2008;
549 Maier and di Pellegrino, 2012; Ito et al., 2017). Not surprisingly, the pgACC is activated during
550 tasks involving social decision-making tasks, which are intuitive and rapid and involve predicting
551 outcomes based on social cues such as facial expression (Apps et al., 2016; Dal Monte et al.,
552 2020). The fact that 'salience'-detecting (sgACC) and 'social/conflict- monitoring' (pgACC)
553 components of the ACC have an overlapping, afferent influence in specific 'hotspots' of the
554 ABmc and Bi, suggests that the internal 'salience' information co-regulates amygdala neurons
555 involved in decision-making networks.
556 The amygdala is involved in an array of functions including fear conditioning and
557 extinction (Phelps et al., 2004; Quirk and Beer, 2006); safety signaling (Genud-Gabai et al.,
558 2013); updating value representations (Buchel et al., 1998); responses to emotion in facial
559 expressions (Breiter et al., 1996; Morris et al., 1996; Fitzgerald et al., 2006), and social decision-
560 making and behavior (Chang et al., 2015; Minxha et al., 2017; Gothard et al., 2018). Current
561 evidence from chronic recordings in monkeys indicates that the amygdala's capacity to
562 participate in all these tasks and contexts is due to a capacity for multi-dimensional processing
563 (Putnam and Gothard, 2019; Pryluk et al., 2020). For example, the same amygdala populations
564 that respond to direct eye gaze (a threat cue in nonhuman primates; Kalin and Shelton, 1989)
565 also respond to non-social aversive stimuli (air-puff). Conversely, neurons that respond to
566 averted eye gaze (a cue predicting submissive, positive social interactions) also respond to juice
567 reward. Amygdala neurons are thus able to flexibly code across social and nonsocial stimuli to
568 predict outcome in specific contexts. The present anatomic findings suggest that this multi-
569 dimensionality may be served by the high rate of converging contacts on the same amygdala
570 neurons from functionally distinct ACC regions, which may confer flexibility across various
571 stimuli and contexts.
572
573 <u>High convergence of sgACC/pgACC contacts on projection neurons</u>
574
575 The majority (85%) of cortical afferent inputs terminate onto pyramidal neurons, based
576 on work in rodents (Brinley-Reed et al., 1995). Synapses located closest to the soma (or on the
577 soma itself) have the most influence on the overall circuit, as they act to strengthen or weaken
578 the overall cellular response (reviewed in; Villa and Nedivi, 2016). One of our most striking
579 findings was that sgACC and pgACC terminals target the same pyramidal cell populations, with
580 relatively few pyramidal neurons having only a single contact. Consistent with this finding,

581 functionally related excitatory inputs are often clustered in regards to synaptic placement along
582 the cell and are thought to possibly contribute to coordinated regulation of synaptic plasticity
583 among co-active inputs (DeBello et al., 2014). Through spatial clustering, temporally co-
584 activated excitatory inputs are more likely to initiate a potentiating response within the cell than
585 inputs spaced a distance from one another. Although we did not examine synaptic contacts onto
586 distal dendrites, the finding that dual contacts at the soma/proximal dendrites were the rule, and
587 were tightly balanced in relationship to one another, strongly suggests cooperative actions in
588 regulating post-synaptic cell excitability. The pgACC and sgACC are separate, but closely
589 related brain regions with respect to connectivity and function. They therefore follow this general
590 principle of "coordinated regulation" by functionally related inputs, contributing to the integration
591 of complex or fluid informational streams.
592 The highly consistent ratio of sgACC to pgACC contacts in normal young animals raises
593 questions about how and when this precise ratio is developed. In mice, the long-range afferents
594 from the medial prefrontal cortex in general arrive in the basal nucleus by postnatal day (PND
595 10-15) (Bouwmeester et al., 2002; Arruda-Carvalho et al., 2017), but synaptic strength
596 continues to develop until PND 30 (early adolescence) based on physiologic data. While the
597 development of the relative 'balance' of the sgACC and pgACC (infralimbic and prelimbic
598 cortices in rodents) terminals on the post-synaptic neuron is not known, experience-dependent
599 plasticity likely contributes (Holtmaat et al., 2006). We speculate that experiences in early life
600 contribute to sgACC:pgACC terminal balance.
601 A factor in the function of terminals is synapse size. Glutamatergic synapses are
602 classified broadly into Class I and Class II synapses (Petrof and Sherman, 2013). Class I
603 synapses are large (> 1 um diameter), associated with large axons, and release glutamate to
604 affect 'all or none' action potentials. They are considered 'drivers' of the circuit. Larger
605 glutamatergic synapses are associated with larger post-synaptic densities (Sheng and Kim,
606 2011), larger axon diameters (Innocenti and Caminiti, 2017) and greater transmitter release
607 (Rosenmund and Stevens, 1996; Murthy et al., 1997). These structural specializations are
608 thought to prioritize functional inputs in terms of timing and signal strength. In contrast, Class II
609 synapses are smaller and modulatory, and shape post-synaptic excitability. In the present study,
610 a higher number of large boutons in sgACC terminals in ABmc and Bi 'hotspots' may confer
611 'driver' function, balanced by pgACC modulators. In future studies, a key question will be to
612 describe sgACC versus pgACC inputs at the ultrastructural level; to determine synaptic size,
613 location (i.e. axo-dendritic spine/shaft, axo-somatic, etc.), and number (i.e single or multiple

614 bouton contacts) (reviewed in, Yang et al., 2018) associated with glutamatergic post-synaptic
615 neurons (Cover and Mathur, 2020).

616 Conclusion

617 The primate amygdala is evolutionarily expanded, accompanied by increased levels of
618 cellular complexity and coding capacity (Grabenhorst et al., 2019; Dal Monte et al., 2020;
619 Gothard, 2020). Consistent with its cellular complexity, divergent coding schemes in the primate
620 amygdala operate to facilitate different functions (Pryluk et al., 2020). Our results may help
621 explain multi-dimensional coding flexibility of amygdala neurons since broad-based sgACC
622 terminal fields appear capable of driving wide-spread activity across the main amygdala nuclei.
623 In contrast, pgACC inputs follow a more restricted, nested topography (Cho et al., 2013)
624 (present results), forming highly convergent contacts on sgACC-recipient neurons in specific
625 subregions. This arrangement allows maximum flexibility, with the sgACC providing broad
626 'internal salience' feedback to the amygdala, but also permitting cooperative signalling with
627 pgACC inputs for conflict monitoring and social decision-making in ‘hotspots’ of convergence.

628 Data sharing statement

629 Digital data can be accessed by contacting the corresponding author at:
630 julie_fudge@urmc.rochester.edu.

631 References

632 Allsop SA et al. (2018) Corticoamygdala Transfer of Socially Derived Information Gates
633 Observational Learning. Cell 173:1329-1342 e1318.
634 Amaral DG, Bassett JL (1989) Cholinergic innervation of the monkey amygdala: An
635 immunohistochemical analysis with antisera to choline acetyltransferase. J Comp Neurol
636 281:337-361.
637 Amemori K, Graybiel AM (2012) Localized microstimulation of primate pregenual cingulate
638 cortex induces negative decision-making. Nature neuroscience 15:776-785.
639 Apps MA, Rushworth MF, Chang SW (2016) The Anterior Cingulate Gyrus and Social
640 Cognition: Tracking the Motivation of Others. Neuron 90:692-707.
641 Arruda-Carvalho M, Wu WC, Cummings KA, Clem RL (2017) Optogenetic Examination of
642 Prefrontal-Amygdala Synaptic Development. The Journal of neuroscience : the official
643 journal of the Society for Neuroscience 37:2976-2985.
644 Ashaber M, Zalanyi L, Palfi E, Stuber I, Kovacs T, Roe AW, Friedman RM, Negyessy L (2020)
645 Synaptic organization of cortico-cortical communication in primates. The European
646 journal of neuroscience 52:4037-4056.
647 Barbas H, Ghashghaei H, Dombrowski SM, Rempel-Clower NL (1999) Medial prefrontal
648 cortices are unified by common connections with superior temporal cortices and

649 distinguished by input from memory-related areas in the rhesus monkey. Journal of
650 Comparative Neurology 410:343-367.
651 Bouwmeester H, Wolterink G, van Ree JM (2002) Neonatal development of projections from the
652 basolateral amygdala to prefrontal, striatal, and thalamic structures in the rat. The
653 Journal of comparative neurology 442:239-249.
654 Breiter HC, Etcoff NL, Whalen PJ, Kennedy WA, Rauch SL, Buckner RL, Strauss MM, Hyman
655 SE, Rosen BR (1996) Response and habituation of the human amygdala during visual
656 processing of facial expression. Neuron 17:875-887.
657 Brinley-Reed M, Mascagni F, McDonald AJ (1995) Synaptology of prefrontal cortical projections
658 to the basolateral amygdala: an electron microscopic study in the rat. Neuroscience
659 letters 202:45-48.
660 Buchel C, Morris J, Dolan RJ, Friston KJ (1998) Brain systems mediating aversive conditioning:
661 an event-related fMRI study. Neuron 20:947-957.
662 Burghy CA, Stodola DE, Ruttle PL, Molloy EK, Armstrong JM, Oler JA, Fox ME, Hayes AS,
663 Kalin NH, Essex MJ, Davidson RJ, Birn RM (2012) Developmental pathways to
664 amygdala-prefrontal function and internalizing symptoms in adolescence. Nature
665 neuroscience 15:1736-1741.
666 Carlsen J, Heimer L (1988) The basolateral amygdaloid complex as a cortical-like structure.
667 Brain research 441:377-380.
668 Carmichael ST, Price JL (1994) Architectonic subdivision of the orbital and medial prefrontal
669 cortex in the macaque monkey. J Comp Neurol 346:366-402.
670 Carmichael ST, Price JL (1995) Limbic connections of the orbital and medial prefrontal cortex in
671 macaque monkeys. J Comp Neurol 363:615-641.
672 Chang SW, Fagan NA, Toda K, Utevsky AV, Pearson JM, Platt ML (2015) Neural mechanisms
673 of social decision-making in the primate amygdala. Proceedings of the National
674 Academy of Sciences of the United States of America 112:16012-16017.
675 Cho YT, Ernst M, Fudge JL (2013) Cortico-Amygdala-Striatal Circuits Are Organized as
676 Hierarchical Subsystems through the Primate Amygdala. The Journal of neuroscience :
677 the official journal of the Society for Neuroscience 33:14017-14030.
678 Chudasama Y, Daniels TE, Gorrin DP, Rhodes SE, Rudebeck PH, Murray EA (2013) The role
679 of the anterior cingulate cortex in choices based on reward value and reward
680 contingency. Cereb Cortex 23:2884-2898.
681 Cover KK, Mathur BN (2020) Axo-axonic synapses: Diversity in neural circuit function. The
682 Journal of comparative neurology.
683 Dal Monte O, Chu CCJ, Fagan NA, Chang SWC (2020) Specialized medial prefrontal-amygdala
684 coordination in other-regarding decision preference. Nature neuroscience 23:565-574.
685 Damasio AR (1996) The somatic marker hypothesis and the possible functions of the prefrontal
686 cortex. Philosophical transactions of the Royal Society of London Series B, Biological
687 sciences 351:1413-1420.
688 DeBello WM, McBride TJ, Nichols GS, Pannoni KE, Sanculi D, Totten DJ (2014) Input clustering
689 and the microscale structure of local circuits. Front Neural Circuits 8:112.
690 Etkin A, Egner T, Peraza DM, Kandel ER, Hirsch J (2006) Resolving emotional conflict: a role
691 for the rostral anterior cingulate cortex in modulating activity in the amygdala. Neuron
692 51:871-882.
693 Fitzgerald DA, Angstadt M, Jelsone LM, Nathan PJ, Phan KL (2006) Beyond threat: amygdala
694 reactivity across multiple expressions of facial affect. NeuroImage 30:1441-1448.
695 Freedman LJ, Insel TR, Smith Y (2000) Subcortical projections of area 25 (subgenual cortex) of
696 the macaque monkey. Journal of Comparative Neurology 421:172-188.
697 Fudge JL, Tucker T (2009) Amygdala projections to central amygdaloid nucleus subdivisions
698 and transition zones in the primate. Neuroscience 159:819-841.

699 Gabard-Durnam LJ, Flannery J, Goff B, Gee DG, Humphreys KL, Telzer E, Hare T, Tottenham
700 N (2014) The development of human amygdala functional connectivity at rest from 4 to
701 23 years: a cross-sectional study. NeuroImage 95:193-207.
702 Gee DG, Bath KG, Johnson CM, Meyer HC, Murty VP, van den Bos W, Hartley CA (2018)
703 Neurocognitive Development of Motivated Behavior: Dynamic Changes across
704 Childhood and Adolescence. The Journal of neuroscience : the official journal of the
705 Society for Neuroscience 38:9433-9445.
706 Genud-Gabai R, Klavir O, Paz R (2013) Safety signals in the primate amygdala. The Journal of
707 neuroscience : the official journal of the Society for Neuroscience 33:17986-17994.
708 Ghashghaei HT, Hilgetag CC, Barbas H (2007) Sequence of information processing for
709 emotions based on the anatomic dialogue between prefrontal cortex and amygdala.
710 NeuroImage 34:905-923.
711 Gothard KM (2020) Multidimensional processing in the amygdala. Nature reviews Neuroscience
712 21:565-575.
713 Gothard KM, Battaglia FP, Erickson CA, Spitler KM, Amaral DG (2007) Neural responses to
714 facial expression and face identity in the monkey amygdala. Journal of neurophysiology
715 97:1671-1683.
716 Gothard KM, Mosher CP, Zimmerman PE, Putnam PT, Morrow JK, Fuglevand AJ (2018) New
717 perspectives on the neurophysiology of primate amygdala emerging from the study of
718 naturalistic social behaviors. Wiley Interdiscip Rev Cogn Sci 9.
719 Grabenhorst F, Baez-Mendoza R, Genest W, Deco G, Schultz W (2019) Primate Amygdala
720 Neurons Simulate Decision Processes of Social Partners. Cell 177:986-998 e915.
721 Holtmaat A, Wilbrecht L, Knott GW, Welker E, Svoboda K (2006) Experience-dependent and
722 cell-type-specific spine growth in the neocortex. Nature 441:979-983.
723 Innocenti GM, Caminiti R (2017) Axon diameter relates to synaptic bouton size: structural
724 properties define computationally different types of cortical connections in primates.
725 Brain structure & function 222:1169-1177.
726 Ito T, Yokokawa K, Yahata N, Isato A, Suhara T, Yamada M (2017) Neural basis of negativity
727 bias in the perception of ambiguous facial expression. Scientific reports 7:420.
728 Johansen-Berg H, Gutman DA, Behrens TE, Matthews PM, Rushworth MF, Katz E, Lozano AM,
729 Mayberg HS (2008) Anatomical connectivity of the subgenual cingulate region targeted
730 with deep brain stimulation for treatment-resistant depression. Cereb Cortex 18:1374-
731 1383.
732 Joyce MKP, Barbas H (2018) Cortical Connections Position Primate Area 25 as a Keystone for
733 Interoception, Emotion, and Memory. The Journal of neuroscience : the official journal of
734 the Society for Neuroscience 38:1677-1698.
735 Kalin NH, Shelton SE (1989) Defensive behaviors in infant rhesus monkeys: environmental
736 cues and neurochemical regulation. Science 243:1718-1721.
737 Kim MJ, Gee DG, Loucks RA, Davis FC, Whalen PJ (2011) Anxiety dissociates dorsal and
738 ventral medial prefrontal cortex functional connectivity with the amygdala at rest. Cereb
739 Cortex 21:1667-1673.
740 Klavir O, Genud-Gabai R, Paz R (2013) Functional connectivity between amygdala and
741 cingulate cortex for adaptive aversive learning. Neuron 80:1290-1300.
742 Livneh U, Resnik J, Shohat Y, Paz R (2012) Self-monitoring of social facial expressions in the
743 primate amygdala and cingulate cortex. Proceedings of the National Academy of
744 Sciences of the United States of America 109:18956-18961.
745 Lockwood PL, Wittmann MK (2018) Ventral anterior cingulate cortex and social decision-
746 making. Neuroscience and biobehavioral reviews 92:187-191.
747 Maier ME, di Pellegrino G (2012) Impaired conflict adaptation in an emotional task context
748 following rostral anterior cingulate cortex lesions in humans. Journal of cognitive
749 neuroscience 24:2070-2079.

McDonald AJ, Muller JF, Mascagni F (2002) GABAergic innervation of alpha type II calcium/calmodulin-dependent protein kinase immunoreactive pyramidal neurons in the rat basolateral amygdala. The Journal of comparative neurology 446:199-218.

Minxha J, Mosher C, Morrow JK, Mamelak AN, Adolphs R, Gothard KM, Rutishauser U (2017) Fixations Gate Species-Specific Responses to Free Viewing of Faces in the Human and Macaque Amygdala. Cell reports 18:878-891.

Modirrousta M, Fellows LK (2008) Dorsal medial prefrontal cortex plays a necessary role in rapid error prediction in humans. The Journal of neuroscience : the official journal of the Society for Neuroscience 28:14000-14005.

Morris JS, Frith CD, Perrett DI, Rowland D, Young AW, Calder AJ, Dolan RJ (1996) A differential neural response in the human amygdala to fearful and happy facial expressions. Nature 383(6603):812-815.

Mosher CP, Zimmerman PE, Gothard KM (2014) Neurons in the monkey amygdala detect eye contact during naturalistic social interactions. Current biology : CB 24:2459-2464.

Munuera J, Rigotti M, Salzman CD (2018) Shared neural coding for social hierarchy and reward value in primate amygdala. Nature neuroscience 21:415-423.

Murthy VN, Sejnowski TJ, Stevens CF (1997) Heterogeneous release properties of visualized individual hippocampal synapses. Neuron 18:599-612.

Neubert FX, Mars RB, Sallet J, Rushworth MF (2015) Connectivity reveals relationship of brain areas for reward-guided learning and decision making in human and monkey frontal cortex. Proceedings of the National Academy of Sciences of the United States of America 112:E2695-2704.

Palomero-Gallagher N, Zilles K (2018) Cyto- and receptor architectonic mapping of the human brain. Handb Clin Neurol 150:355-387.

Palomero-Gallagher N, Eickhoff SB, Hoffstaedter F, Schleicher A, Mohlberg H, Vogt BA, Amunts K, Zilles K (2015) Functional organization of human subgenual cortical areas: Relationship between architectonical segregation and connectional heterogeneity. NeuroImage 115:177-190.

Petrof I, Sherman SM (2013) Functional significance of synaptic terminal size in glutamatergic sensory pathways in thalamus and cortex. The Journal of physiology 591:3125-3131.

Phelps EA, Delgado MR, Nearing KI, LeDoux JE (2004) Extinction learning in humans: role of the amygdala and vmPFC. Neuron 43:897-905.

Pitkanen A, Amaral DG (1993) Distribution of parvalbumin-immunoreactive cells and fibers in the monkey temporal lobe: the amygdaloid complex. The Journal of comparative neurology 331:14-36.

Pryluk R, Shohat Y, Morozov A, Friedman D, Taub AH, Paz R (2020) Shared yet dissociable neural codes across eye gaze, valence and expectation. Nature 586:95-100.

Putnam PT, Gothard KM (2019) Multidimensional Neural Selectivity in the Primate Amygdala. eNeuro 6.

Quirk GJ, Beer JS (2006) Prefrontal involvement in the regulation of emotion: convergence of rat and human studies. Curr Opin Neurobiol 16:723-727.

Reddan MC, Wager TD, Schiller D (2018) Attenuating Neural Threat Expression with Imagination. Neuron 100:994-1005 e1004.

Rosenmund C, Stevens CF (1996) Definition of the readily releasable pool of vesicles at hippocampal synapses. Neuron 16:1197-1207.

Rudebeck PH, Buckley MJ, Walton ME, Rushworth MF (2006) A role for the macaque anterior cingulate gyrus in social valuation. Science 313:1310-1312.

Rudebeck PH, Putnam PT, Daniels TE, Yang T, Mitz AR, Rhodes SE, Murray EA (2014) A role for primate subgenual cingulate cortex in sustaining autonomic arousal. Proceedings of the National Academy of Sciences of the United States of America 111:5391-5396.

Rushworth MFS, Mars RB, Sallee J (2013) Are there specialized circuits for social cognition and are they unique to humans? Curr Opin Neurobiol 23:436-442.

Rutishauser U, Mamelak AN, Adolphs R (2015) The primate amygdala in social perception - insights from electrophysiological recordings and stimulation. Trends in neurosciences 38:295-306.

Rutishauser U, Tudusciuc O, Neumann D, Mamelak AN, Heller AC, Ross IB, Philpott L, Sutherling WW, Adolphs R (2011) Single-unit responses selective for whole faces in the human amygdala. Current biology : CB 21:1654-1660.

Schneider CA, Rasband WS, Eliceiri KW (2012) NIH Image to ImageJ: 25 years of image analysis. Nat Methods 9:671-675.

Sharma KK, Kelly EA, Pfeifer CW, Fudge JL (2020) Translating Fear Circuitry: Amygdala Projections to Subgenual and Perigenual Anterior Cingulate in the Macaque. Cereb Cortex 30:550-562.

Sheng M, Kim E (2011) The postsynaptic organization of synapses. Cold Spring Harbor perspectives in biology 3.

Stephan H, Frahm HD, Baron G (1987) Comparison of brain structure volumes in insectivora and primates VII. Amygdaloid components. J Hirnforsch 5:571-584.

Van Hoesen GW, Morecraft RJ, Vogt BA (1993) Connections of the monkey cingulate cortex. In: Neurobiology of Cingulate Cortex and Limbic Thalamus: A Comprehensive Treatise (Vogt BA, Gabriel M, eds), pp 249-284. Boston: Birkhauser.

Villa KL, Nedivi E (2016) Excitatory and Inhibitory Synaptic Placement and Functional Implications. In, pp 467-487. Japan: Soringer.

Vogt BA (2005) Pain and emotion interactions in subregions of the cingulate gyrus. Nature reviews Neuroscience 6:533-544.

Vogt BA, Vogt L, Farber NB, Bush G (2005) Architecture and neurocytology of monkey cingulate gyrus. The Journal of comparative neurology 485:218-239.

Wang S, Tudusciuc O, Mamelak AN, Ross IB, Adolphs R, Rutishauser U (2014) Neurons in the human amygdala selective for perceived emotion. Proceedings of the National Academy of Sciences of the United States of America 111:E3110-3119.

Wang S, Yu R, Tyszka JM, Zhen S, Kovach C, Sun S, Huang Y, Hurlemann R, Ross IB, Chung JM, Mamelak AN, Adolphs R, Rutishauser U (2017) The human amygdala parametrically encodes the intensity of specific facial emotions and their categorical ambiguity. Nature communications 8:14821.

Wouterlood FG, Boekel AJ, Meijer GA, Belien JA (2007) Computer-assisted estimation in the CNS of 3D multimarker 'overlap' or 'touch' at the level of individual nerve endings: a confocal laser scanning microscope application. Journal of neuroscience research 85:1215-1228.

Yang Y, Lu J, Zuo Y (2018) Changes of synaptic structures associated with learning, memory and diseases. Brain Science Advances 4(2):99-117.

Zhang W, Schneider DM, Belova MA, Morrison SE, Paton JJ, Salzman CD (2013) Functional circuits and anatomical distribution of response properties in the primate amygdala. The Journal of neuroscience : the official journal of the Society for Neuroscience 33:722-733.

843 **Figures Legends**

844 Table 1. Experimental cases.

845 Figure 1.

846 **Histological markers for boundary designations.** (A-D) Acetylcholinesterase (AChE) stained
847 sections of *Macaque fasicularis* amygdala. (E-F) Identification of intercalated cell masses
848 (ICMs) following anti-tracer immunohistochemistry with Nissl counterstain. * denote ICMs
849 bordering amygdala nuclei. Abbreviations: **AAA**, anterior amygdaloid area; **ABmc**,
850 magnocellular subdivision of the accessory basal nucleus; **ABpc**, parvocellular subdivision of
851 the accessory basal nucleus; **AC**, anterior commissure; **AHA**, amygdalohippocampal area;
852 **Astr**, amygdalostriatal area; **Bi**, intermediate division of the basal nucleus; **Bmc**, magnocellular
853 division of the basal nucleus; **Bpc**, parvocellular division of the basal nucleus; **CeM**, central
854 nucleus, medial subdivision; **CeLcn**, central nucleus, lateral subdivision; **CoA**, anterior cortical
855 nucleus; **H**, hippocampus; **L**, lateral nucleus; **M**, medial nucleus; **oc**, optic chiasm; **ot**, optic tract;
856 **P**, putamen; **PAC**, periamygdaloid complex; **V**, ventricle. Scale bar= A,E= 500 um; F= 200 um.
857

858 Figure 2.

859 **Triple immunofluorescence analysis: criteria for spot/surface contact.** In Imaris
860 software, spot/surface contacts are based on a measurement from the center of the spot (spot^{r})
861 to the edge of the rendered surface object. As 'spots" were calculated as 2um, a radius of 1um
862 would determine all spots "touching" a surface (pink line). Our analysis was restricted to a
863 maximum object to surface distance of 0.5um (red line) (approximately 50% overlap of spots
864 and surfaces). Scale bar= 0.5 um.

865 Figure 3.

866 **Locations of the sgACC (area 25/14c) and pgACC (area 24b, 32) injection sites in**
867 **sagittal section of the prefrontal cortex** (assessed using cytoarchitectural criteria of
868 Carmichael and Price, 1994). (A) Cytoarchitectural shifts across the medial prefrontal cortex,
869 including the ACC. Agranular (blue), dysgranular (green) and granular (red). (B) Sagittal
870 schematic of showing placement of anterograde injection sites. (C) Case 37FR, with a single
871 injection into area 25r, and adjacent cresyl violet stained section. (D1, D2) Brightfield images of

872 dual tracer injections into pgACC (area 32, 53FS) (D1) and sgACC (area 25/14c, 53FR) (D2) in
873 the same hemisphere of Case 53. (Following the area 25 injection, anterogradely labeled fibers
874 are seen leaving the cortex, and entering the ventral striatum). Adjacent NeuN-immunostained
875 sections show respective the cytoarchitectural features at each site. Arrowheads delineate
876 dysgranular layer IV in area 32 (D1).

877 Figure 4.

878 **General topography of anterogradely labeled fibers in two different cases after**
879 **injections into sgACC and pgACC.** Fiber distribution following injections into sgACC (case
880 37FR, blue; A-C) and pgACC (case 46FR, red; D-F). ***Abbrs.*** **ABmc**, accessory basal nucleus,
881 magnocellular subdivision; **ABpc**, accessory basal nucleus, parvicellular subdivision; **ABs**,
882 accessory basal nucleus, sulcal subdivision; **AC**, anterior commissure; **AHA**,
883 amygdalohippocampal region; **Bi**, basal nucleus, intermediate subdivision; **Bmc**, basal nucleus,
884 magnocellular subdivision; **Bpc**, basal nucleus, parvicellular subdivision; **CeLcn**, lateral
885 subdivision of the central nucleus; **H**, hippocampus; **L**, lateral nucleus; **M**, medial nucleus;
886 **mAstr**, medial amygdalostriatal area; **OT**, optic tract; **P**, putamen; **V**, ventricle;

887 Figure 5.

888 **Anterogradely labeled fiber distribution in the main amygdala nuclei following paired pg-**
889 **and sgACC tracer injections.** Rostral to caudal distribution of sgACC (blue) and pgACC (red)
890 fibers in Case 46 (A-C) and 53 (D-F). A-F. Areas of sgACc/pgACC overlap are circled in green;
891 areas of sgACC non-overlap area circled in dark blue. G-H. Inverted dark-field micrograph of
892 fiber termination in sgACC (G) and pgACC (H) at 20X magnification. Single headed arrows
893 denote thick, beaded labeled fibers that were seen in the sgACC projection. Double-headed
894 arrows show thin, beaded labeled fibers found in both the pgACC and sgACC projection field.
895 Fiber density measures in each 'hotspot' for sgACC (blue) vs pgACC (red). See Extended data
896 Figure 5.1 for labeled fiber distribution including the extended amygdala.

897 Extended data Figure 5-1.

898 **Anterogradely labeled fiber distribution following *paired* pg- and sgACC tracer**
899 **injections, including extended amygdala regions.** Rostral to caudal distribution of sgACC
900 (blue) and pgACC (red) fibers in Case 46 (A-C) and 53 (D-F).

901 Figure 6.

902 **Triple immunofluorescent analysis and quantification of tracer contacts following**
903 **paired pgACC/sgACC injections.** (A) Camera lucida rendering of anterograde fiber distribution
904 following pgACC (red) and sgACC (green) injections, used for selection and registration of
905 'hotspots' in the ABmc and Bi (boxed areas). (B) CAMK-IIα (blue), fluoroscein tracer (FS) and
906 fluoruby tracer (FR) triple immunofluorescent confocal micrograph collected in the ABmc
907 'hotpspot', boxed area in A. Scale bar = 10 um (C) Overlay of Imaris software 'surface' (CAMK-
908 IIα) and 'spot' (tracer) renderings onto confocal micrograph (shown in B). Scale bar = 10 um
909 (D) Imaris rendered objects depicting sites of tracer contact with CAMK-IIα cells. (E) The
910 proportion of pgACC/sgACC contacts onto all CAMK-IIα cells counted in the ABmc and Bi
911 'hotspots'. (F) The proportion of CAMK-IIα cells with no contact, single contacts, or dual
912 contacts from pgACC and sgACC anterogradely labeled fibers in the ABmc and Bi (****=
913 $p<0.001$, two-way ANOVA with Tukey multiple comparisons post hoc test). See Extended data
914 Figure 6-1 for raw counts and ratios of sgACC and pgACC contacts by region of interest and
915 rostrocaudal level, and Extended data Figure 6-2 for pooled raw counts and ratios of pgACC
916 and sgACC contacts by case and region of interest.

917 Extended data Figure 6-1.

918 Rostro-caudal levels: Raw counts and ratios of sgACC and pgACC contacts onto CAMK-
919 IIα cells in each case by region of interest at 3 rostrocaudal levels. No rostrocaudal differences
920 were found. Two-way ANOVA with Tukey Multiple Comparisons test, $F(5,16)= 0.2176$,
921 $p=0.9495$).

922 Extended data Figure 6-2.

923 Raw counts and ratios of pgACC and sgACC contacts onto CAMK-IIα cells by case and
924 region of interest. No rostrocaudal differences were found. One-Way ANOVA with Tukey
925 multiple comparisons tests, Case 46:ABmc= $F(2,4)=11.85$, $p=0.0609$; Case 46:Bi=
926 $F(2,3)=6.231$, $p=0.0855$; Case 53:ABmc= $F(2,5)=5.136$, $p=0.0613$, $p=0.0613$; Case 53:Bi=
927 $F(2,6)=0.5588$, $p=0.5990$)

928 Figure 7.

929 **The proportion of pgACC to sgACC dual contacts are tightly balanced in**
930 **amygdalar hotspots.** (A) Binned ratios of pgACC/sgACC contacts onto individual dual-
931 contacted CAMK-IIα cells. A large percentage of CAMK-IIα cells had ratios 1:1 pgACC-to-
932 sgACC contacts (gray bars) in both the ABmc and Bi. (B) Frequency distribution of
933 pgACC/sgACC contacts onto CAMK-IIα cells. Ratio bins range from 0 to >3.5. (C) Quantitative
934 comparisons of ratio bin counts (*=p<0.05,****= p<0.001, one-way ANOVA with Tukey multiple
935 comparisons post hoc test). See Extended data Figure 7-1 for raw bin counts of dual contact per
936 CAMK-IIα cell by case and region, and quantitative comparisons across bins.

937 Extended data Figure 7-1.

938 Raw bin counts of pgACC/sgACC dual contacts onto CAMK-IIα cells by case and region
939 of interest. Quantitative comparisons of ratio bin counts display significantly higher counts in the
940 range of 1-1.5 when compared to every other bin (*=p<0.05, ****= p<0.001, one-way ANOVA
941 with Tukey multiple comparisons post hoc test).

942 Figure 8.

943 **Unbiased stereology and quantitative analysis of anterogradely labeled synaptic**
944 **boutons at 100x.** (A) Frequency bin representation of volumetric measurements of tracer-
945 labeled synaptic boutons from the sgACC (blue) and pgACC (red) in 'hotspots' , and sgACC
946 terminal boutons in non-overlapping AHA (gray dashed) and Lateral nucleus regions (black
947 dashed) (for comparison). Volume bins ranged from 0->3.45 um^3. Many boutons fell below 0.52
948 um^3 for all projections (arrow denotes shift to large categorized boutons). (B) A representative
949 brightfield micrograph of anterograde tracer-labeled fibers in the basal nucleus 'hotspot'
950 showing bouton types. Terminal boutons (single arrowhead) were characterized by a distinct
951 swelling with an apparent stalk emanating from the axon terminal. *En passant boutons* (double
952 arrowhead) displayed a characteristic swelling along the terminal fiber. Scale bar= 25 um. (C-D)
953 Log frequency of small (black bars) vs large bouton (white bars) comparisons for each case with
954 paired injections: (C) Case 46 (areas 24/25) (D) Case 53 (areas 32/25) (E) Pooled analyses,
955 both cases. Multiple comparison tests were performed to compare small vs. large bouton
956 across region and case. In all situations, there were significantly more small boutons compared
957 to large boutons (p=0.008 [J46], p=0.015 [J53], p=0.005 [pooled]). Large boutons (greater than

958 0.52 um^3 volume) were significantly more frequent on axons originating from sgACC in hotspots,
959 but not non-overlapping regions. (One-way ANOVA with Tukey multiple comparisons, F(2,3)=
960 96.18, p= 0.0019; sgACC vs pgACC= p=0.0030; sgACC vs non-OL= p=0.0023). Extended data
961 Figure 8-1 shows raw data counts of bouton type. Extended data Figure 8-2 shows regional
962 counts of bouton size across injection source (pgACC, 32/24; sgACC, 25; sgACC, non-OL
963 regions) and ROI (ABmc, Bi, AHA and LA).

964 Extended data Figure 8-1.

965 Regional counts of small (<0.52 um^3) and large (>0.52 um^3) boutons across paired
966 cases (Case 46, 24/25 injections; Case 53, 32/25 injections), injection source (pgACC, 32/24;
967 sqACC, 25; sgACC (non-OL; AHA and LA) and ROI (ABmc, Bi, AHA, and LA). We found that
968 the sgACC terminals that overlapped pgACC-containing sites had significantly more large
969 boutons (27-31%) compared to the pgACC (9-10%) [*sgACC*: J46 (total large boutons/total) =
970 194/617; M53 (total large boutons/total) = 142/509; *pgACC*: J46 (total large boutons/total) =
971 29/307; M53 (total large boutons/total) = 61/595; p=0.003; One-Way ANOVA with Tukey's
972 multiple comparison test, F(2,3)=96.18= p=0.0019; sgACC vs pgACC= p=0.0003].

973 Extended data Figure 8-2.

974 Regional counts of small (<0.52 um^3) and large (>0.52 um^3) boutons across injection
975 source (pgACC, 32/24; sgACC, 25; sgACC, non-OL regions) and ROI (ABmc, Bi, AHA and LA).
976 'Large' bouton comparisons from the same afferent source did not differ significantly across the
977 ABmc, Bi (p=0.0.3739, Two-way ANOVA, F(2,2)=1.674). sgACC non-OL areas had significantly
978 fewer large boutons (Tukey Multiple Comparisons test following one-way ANOVA; sgACC vs
979 non-OL= p=0.0023).
980

Case	Age (yrs)	Wt (kg)	Target	Hemisphere	Tracer	Tracer Vol
37	3.7	4.3	25r	L	FR	40
***46**	3.2	4.9	24b	L	FR	40
***46**	3.2	4.9	25r/c	L	FS	40
50	4.25	4.7	25r/c	L	FR	40
***53**	5.9	5.5	32r/c	L	FS	40
***53**	5.9	5.5	25c,14	R	FR	40
54	3.3	5	32r/c, 24b	R	FS	150

* denotes part of an injection pair

Table 1

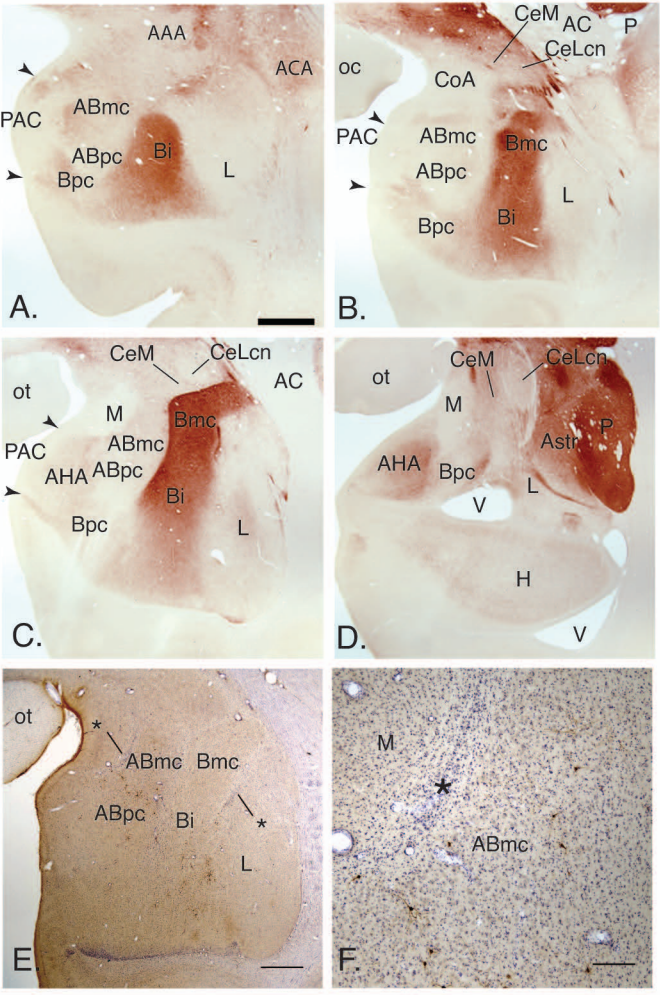
AAA
ACA
PAC
ABmc
ABpc
Bi
Bpc
L
A.
CeM
AC
P
CeLcn
oc
CoA
PAC
ABmc
Bmc
ABpc
L
Bi
Bpc
B.
CeM
CeLcn
ot
AC
M
Bmc
PAC
ABmc
AHA
ABpc
Bi
Bpc
L
C.
CeM
CeLcn
ot
M
Astr
P
AHA
Bpc
L
V
H
V
D.
ot
*
ABmc
Bmc
ABpc
Bi
*
L
E
M
*
ABmc
F.

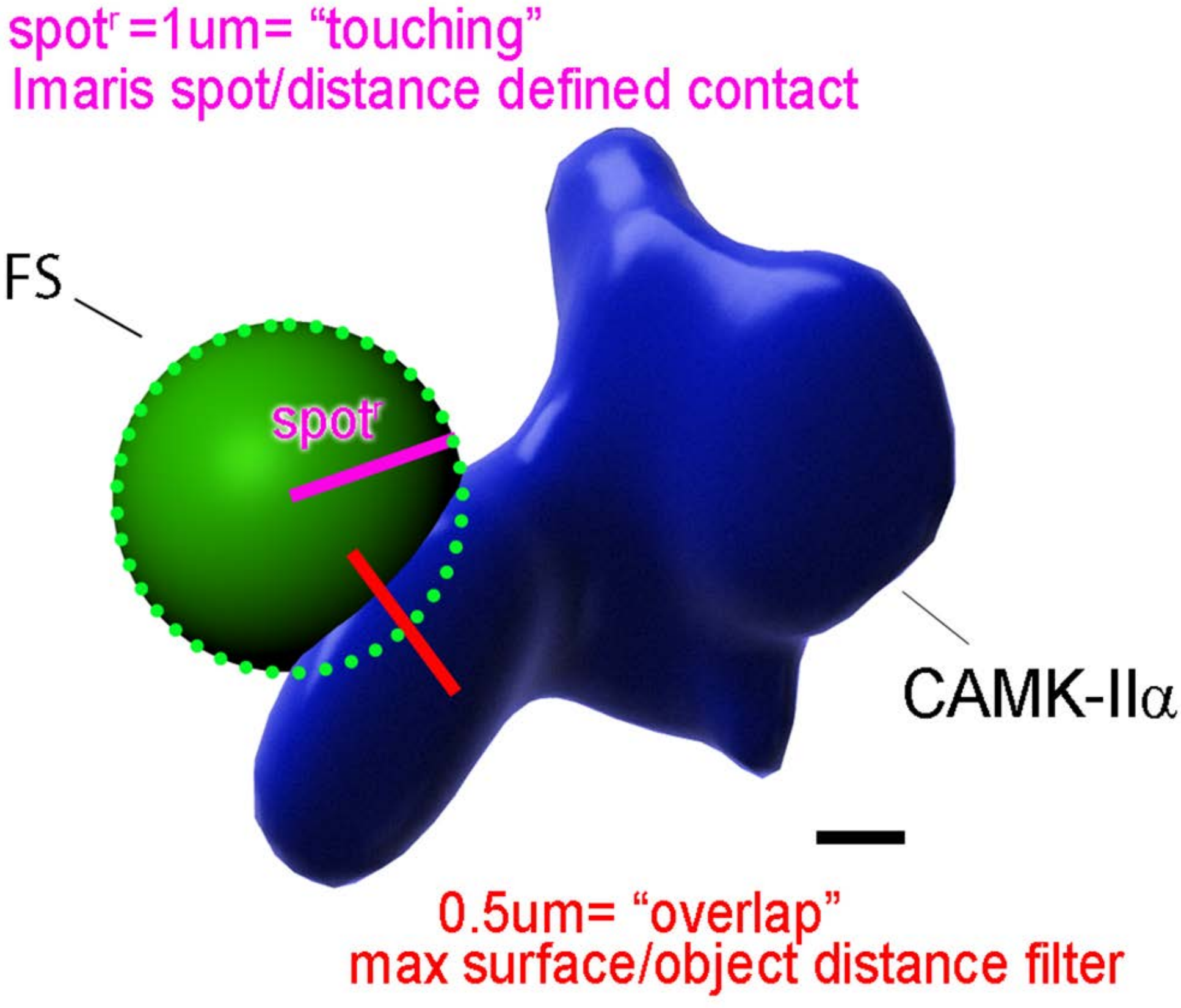
spot^r =1um= "touching"
Imaris spot/distance defined contact
FS
spot^r
CAMK-IIα
0.5um= "overlap"
max surface/object distance filter

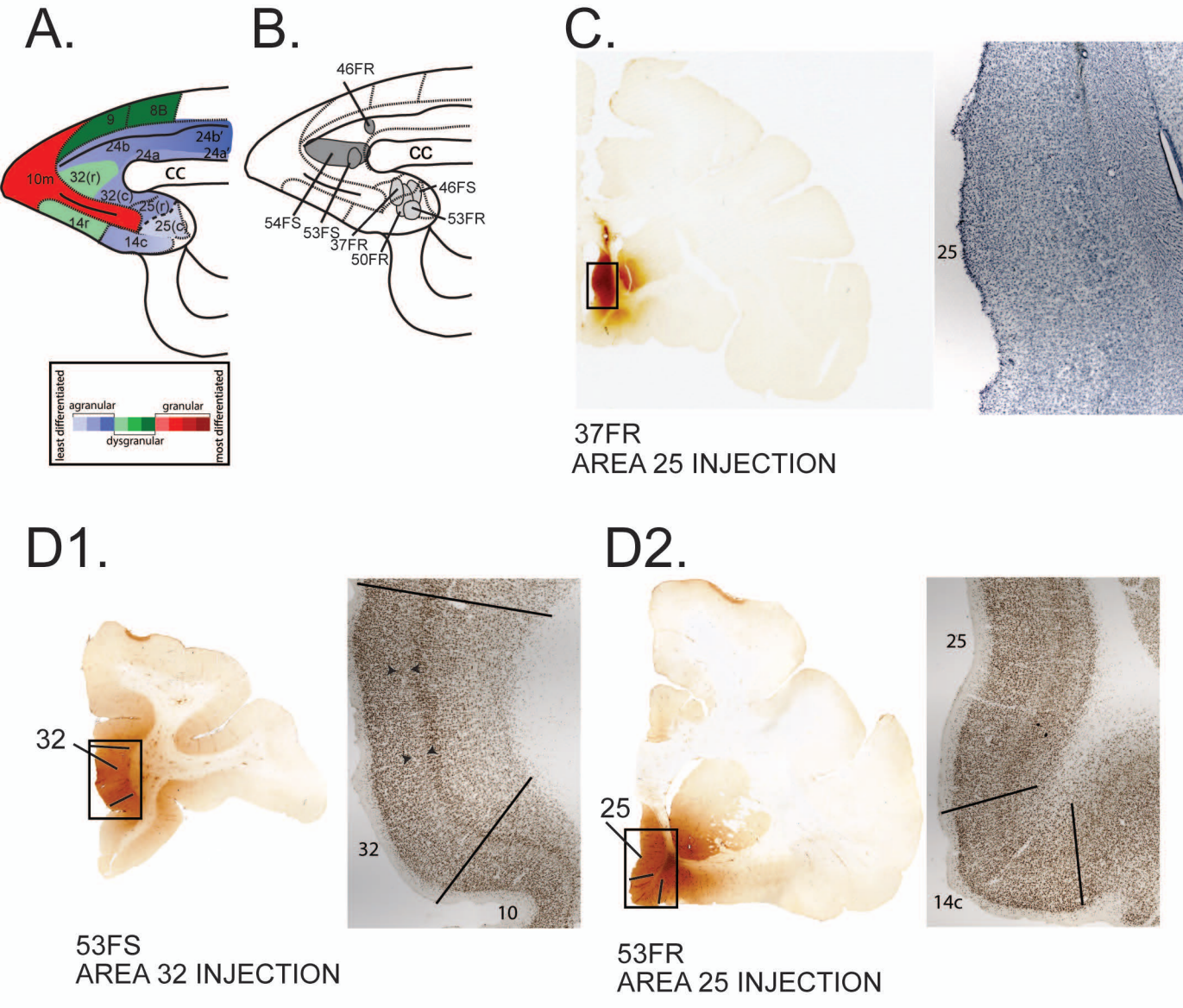
A.
9
8B
24b
24b'
24a
24a'
10m
32(r)
CC
32(c)
25(r)
25(c)
14r
14c
least differentiated
agranular
granular
dysgranular
most differentiated
B.
46FR
CC
46FS
54FS
53FS
37FR
50FR
53FR
C.
25
37FR
AREA 25 INJECTION
D1.
32
32
10
53FS
AREA 32 INJECTION
D2.
25
25
14c
53FR
AREA 25 INJECTION

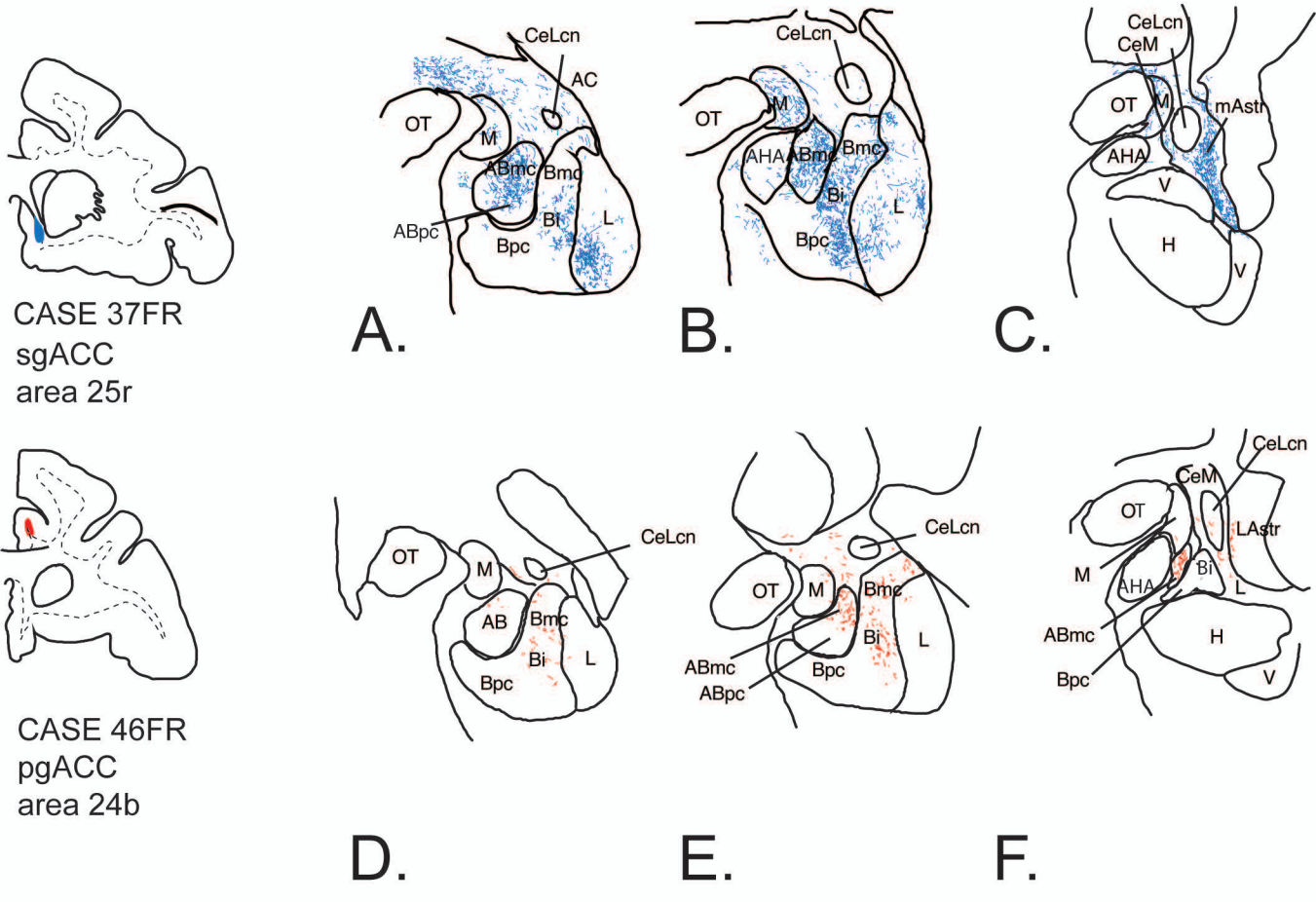
CASE 37FR
sgACC
area 25r
CASE 46FR
pgACC
area 24b
A.
B.
C.
D.
E.
F.
CeLcn
AC
OT
M
ABmc
Bmc
ABpc
Bi
Bpc
L
AHA
CeM
mAstr
V
H
AB
LAstr

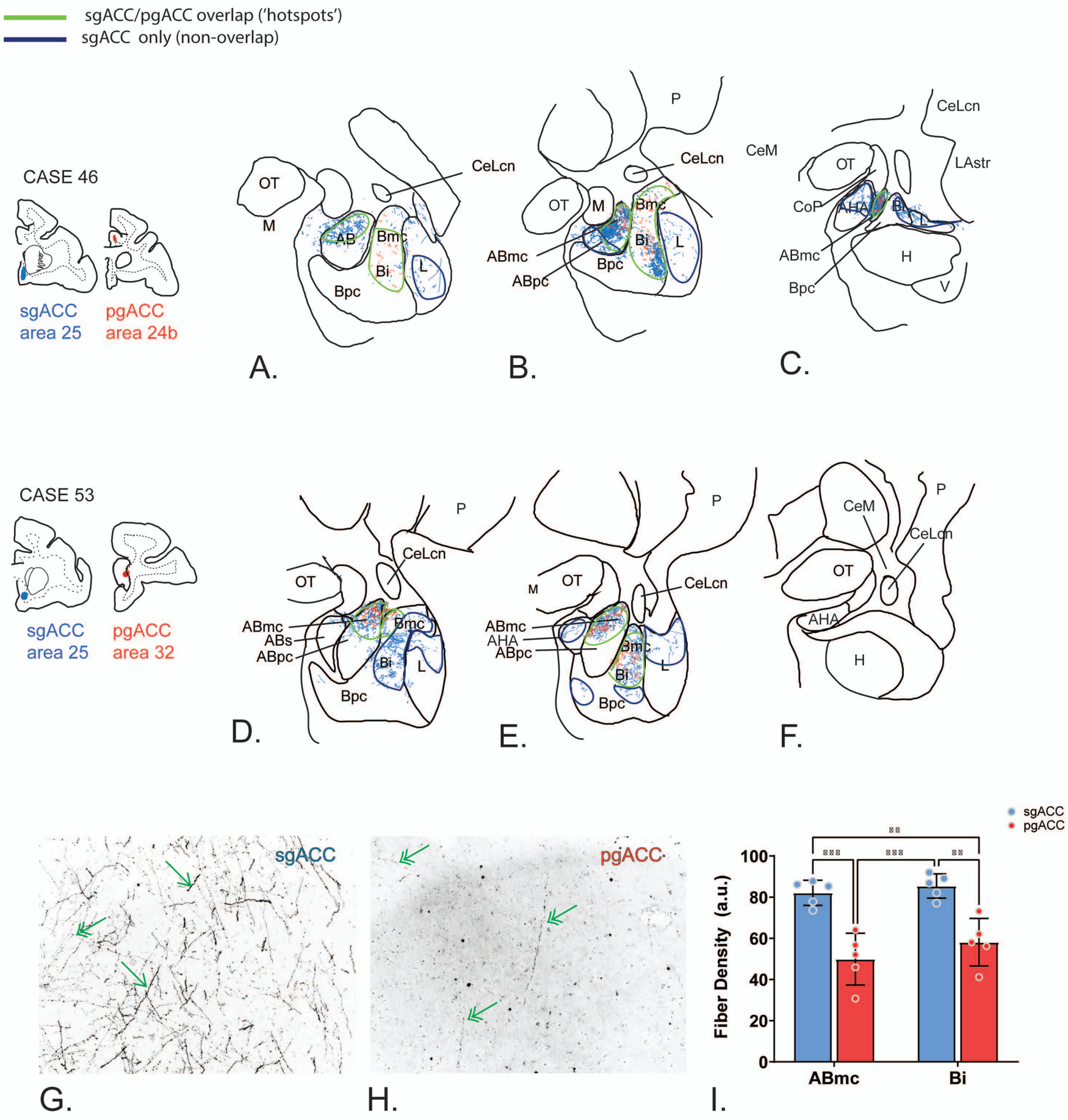
sgACC/pgACC overlap ('hotspots')
sgACC only (non-overlap)
CASE 46
sgACC
area 25
pgACC
area 24b
OT
M
CeLcn
AB
Bmc
Bi
L
Bpc
A.
P
CeLcn
OT
M
Bmc
ABmc
ABpc
Bi
L
Bpc
B.
CeLcn
CeM
OT
LAstr
CoP
AHA
Bi
L
ABmc
H
Bpc
V
C.
CASE 53
sgACC
area 25
pgACC
area 32
P
CeLcn
OT
ABmc
ABs
ABpc
Bmc
Bi
L
Bpc
D.
P
M
OT
CeLcn
ABmc
AHA
ABpc
Bmc
Bi
L
Bpc
E.
P
CeM
CeLcn
OT
AHA
H
F.
sgACC
pgACC
G.
H.
sgACC
pgACC
Fiber Density (a.u.)
100
80
60
40
20
0
ABmc
Bi
I.

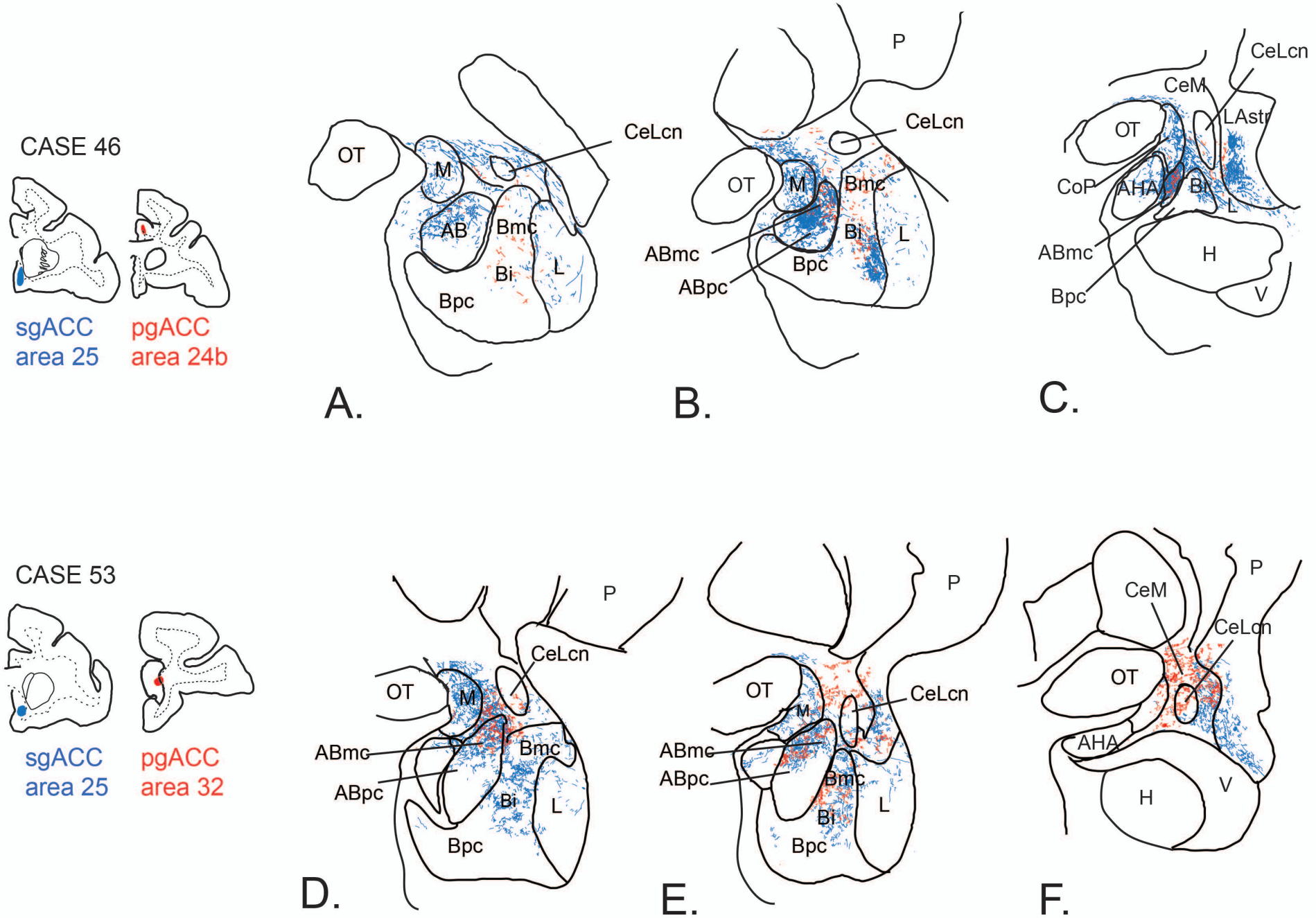
CASE 46
sgACC
area 25
pgACC
area 24b
OT
M
AB
Bmc
Bi
Bpc
L
CeLcn
A.
P
OT
M
Bmc
Bi
Bpc
L
ABmc
ABpc
CeLcn
B.
CeLcn
CeM
LAstr
OT
CoP
AHA
Bi
L
ABmc
Bpc
H
V
C.
CASE 53
sgACC
area 25
pgACC
area 32
P
CeLcn
OT
M
ABmc
ABpc
Bmc
Bi
L
Bpc
D.
P
OT
M
CeLcn
ABmc
ABpc
Bmc
Bi
L
Bpc
E.
P
CeM
CeLcn
OT
AHA
H
V
F.

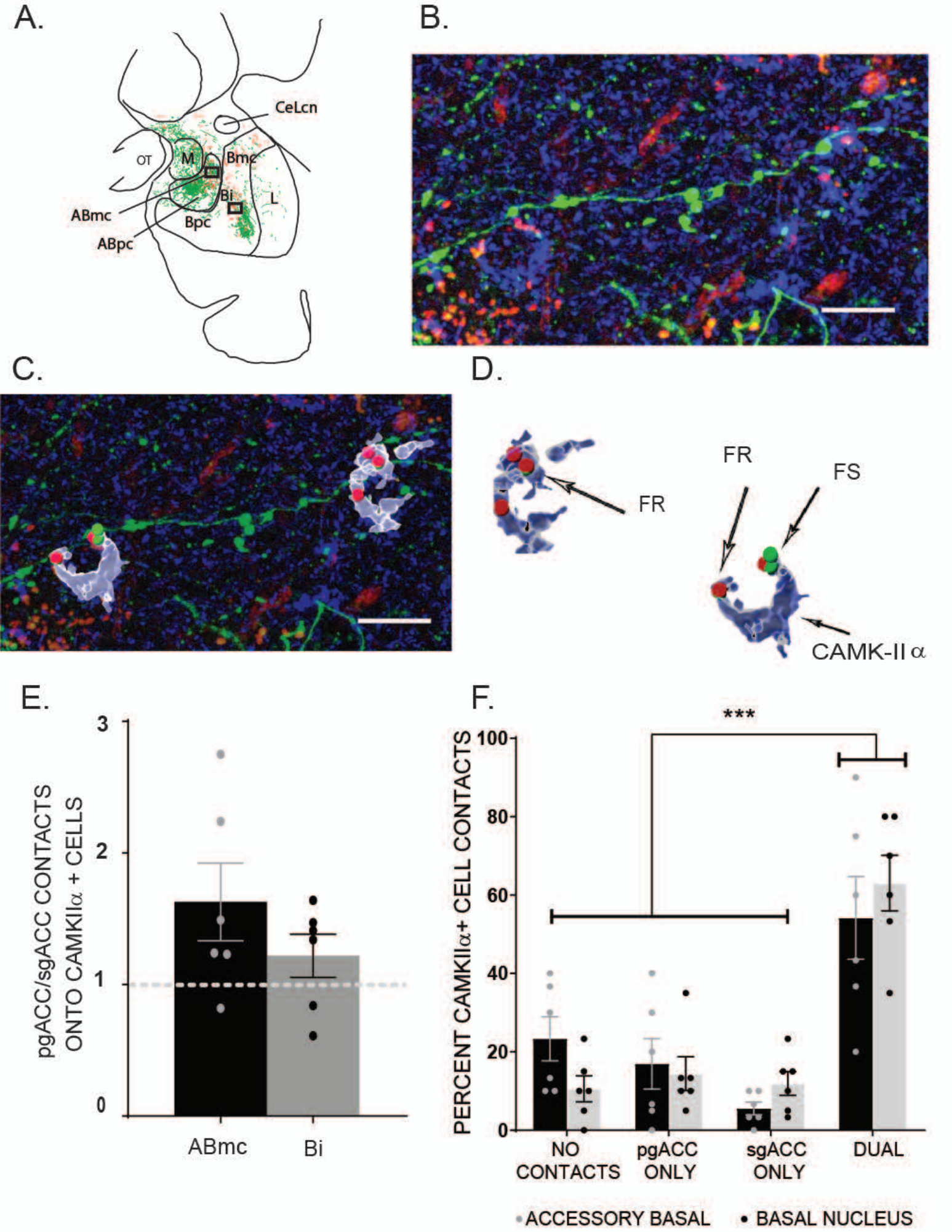
A.
CeLcn
OT
M
Bmc
Bi
L
ABmc
Bpc
ABpc
B.
C.
D.
FR
FR
FS
CAMK-II α
E.
pgACC/sgACC CONTACTS
ONTO CAMKIIα + CELLS
3
2
1
0
ABmc
Bi
F.
***
PERCENT CAMKIIα+ CELL CONTACTS
100
80
60
40
20
0
NO
CONTACTS
pgACC
ONLY
sgACC
ONLY
DUAL
ACCESSORY BASAL
BASAL NUCLEUS

J46	**RAW COUNTS**		**RATIO**	J46	**RAW COUNTS**		**RATIO**
ABmc	pgACC	sgACC	**pgACC/sgACC**	Bi	pgACC	sgACC	**pgACC/sgACC**
ROSTAL	122	82	1.49	*ROSTAL*	51	36	1.42
MEDIAL	22	8	2.75	*MEDIAL*	41	49	0.84
CAUDAL	65	29	2.24	*CAUDAL*	23	14	1.64
J53	**RAW COUNTS**		**RATIO**	J53	**RAW COUNTS**		**RATIO**
ABmc	pgACC	sgACC	**pgACC/sgACC**	Bi	pgACC	sgACC	**pgACC/sgACC**
ROSTAL	41	33	1.24	*ROSTAL*	56	38	1.47
MEDIAL	43	52	0.83	*MEDIAL*	37	60	0.62
CAUDAL	53	43	1.23	*CAUDAL*	63	47	1.34

Table 6.1

	RAW COUNTS		RATIO
ABmc	pgACC	sgACC	**pgACC/sgACC**
J46	209	119	1.76
J53	137	128	1.07

Bi	pgACC	sgACC	**pgACC/sgACC**
J46	115	99	1.16
J53	156	145	1.08

Table 6-2.

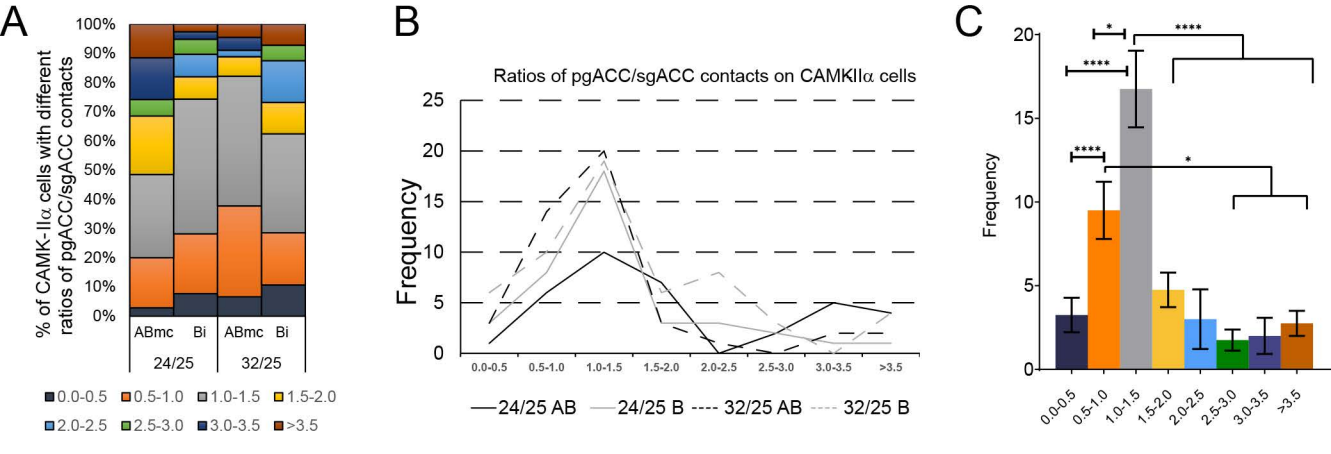
A
100%
90%
80%
70%
60%
50%
40%
30%
20%
10%
0%
% of CAMK-IIα cells with different ratios of pgACC/sgACC contacts
ABmc
Bi
ABmc
Bi
24/25
32/25
0.0-0.5
0.5-1.0
1.0-1.5
1.5-2.0
2.0-2.5
2.5-3.0
3.0-3.5
>3.5
B
Ratios of pgACC/sgACC contacts on CAMKIIα cells
Frequency
25
20
15
10
5
0
0.0-0.5
0.5-1.0
1.0-1.5
1.5-2.0
2.0-2.5
2.5-3.0
3.0-3.5
>3.5
24/25 AB
24/25 B
32/25 AB
32/25 B
C
Frequency
20
15
10
5
0
*
****
****
****
*
0.0-0.5
0.5-1.0
1.0-1.5
1.5-2.0
2.0-2.5
2.5-3.0
3.0-3.5
>3.5

		0.0-0.5	0.5-1.0	1.0-1.5	1.5-2.0	2.0-2.5	2.5-3.0	3.0-3.5	>3.5
MF46 (24b/25)	ABmc	1.00	6.00	10.00	7.00	0.00	2.00	5.00	4.00
	Bi	3.00	8.00	18.00	3.00	3.00	2.00	1.00	1.00
MF53 (32/25)	ABmc	3.00	14.00	20.00	3.00	1.00	0.00	2.00	2.00
	Bi	6.00	10.00	19.00	6.00	8.00	3.00	0.00	4.00

Table 7-1

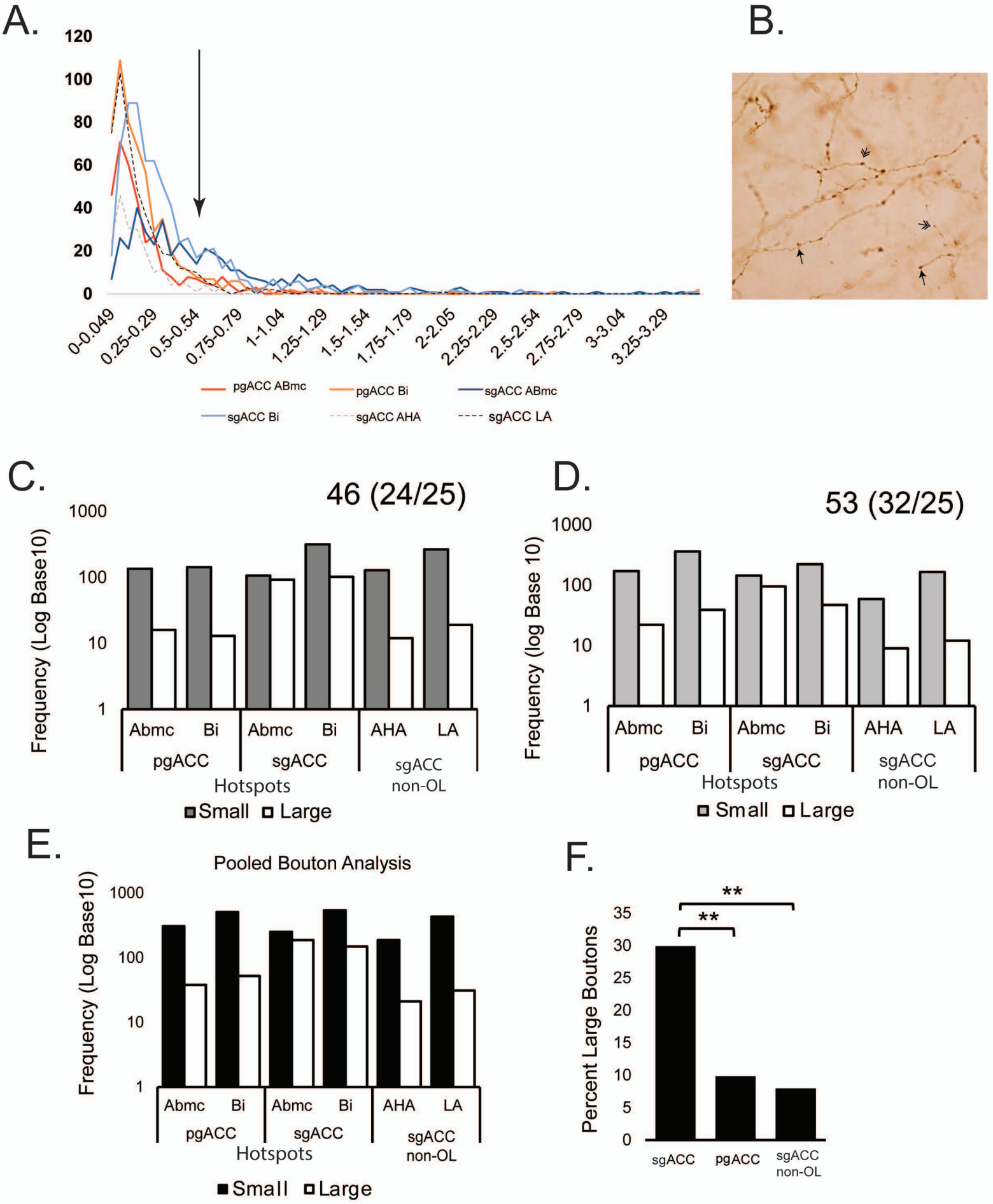
A.
120
100
80
60
40
20
0
0-0.049
0.25-0.29
0.5-0.54
0.75-0.79
1-1.04
1.25-1.29
1.5-1.54
1.75-1.79
2-2.05
2.25-2.29
2.5-2.54
2.75-2.79
3-3.04
3.25-3.29
pgACC ABmc
pgACC Bi
sgACC ABmc
sgACC Bi
sgACC AHA
sgACC LA
B.
C.
46 (24/25)
Frequency (Log Base10)
1000
100
10
1
Abmc
Bi
Abmc
Bi
AHA
LA
pgACC
sgACC
sgACC non-OL
Hotspots
Small
Large
D.
53 (32/25)
Frequency (log Base 10)
1000
100
10
1
Abmc
Bi
Abmc
Bi
AHA
LA
pgACC
sgACC
sgACC non-OL
Hotspots
Small
Large
E.
Pooled Bouton Analysis
Frequency (Log Base10)
1000
100
10
1
Abmc
Bi
Abmc
Bi
AHA
LA
pgACC
sgACC
sgACC non-OL
Hotspots
Small
Large
F.
Percent Large Boutons
35
30
25
20
15
10
5
0
**
**
sgACC
pgACC
sgACC non-OL

Table 8-1

		Small	Large	TOTAL
MFJ46				
pgACC	Abmc	135	16	151
	Bi	143	13	156
TOTAL		278	29	**307**
MFJ46				
sgACC	Abmc	106	92	198
	Bi	317	102	419
TOTAL		423	194	**617**
MFJ46				
sgACC Non-OL	AHA	128	12	140
sgACC Non-OL	LA	265	19	284
TOTAL		393	31	**424**
MFJ53				
pgACC	Abmc	171	22	193
	Bi	363	39	402
TOTAL		534	61	**595**
MFJ53				
sgACC	Abmc	144	95	239
	Bi	223	47	270
TOTAL		367	142	**509**
MFJ53				
sgACC Non-OL	AHA	59	9	68
sgACC Non-OL	LA	165	12	177
TOTAL		224	21	**245**

Table 8-2.

		Small	Large	TOTAL
pgACC	Abmc	306	38	344
	Bi	506	52	558
	TOTAL	812	90	**902**
sgACC	Abmc	250	187	437
	Bi	540	149	689
	TOTAL	790	336	**1126**
sgACC Non- OL	AHA	187	21	208
	LA	430	31	461
	TOTAL	617	52	**669**